

Total variance based feature point selection and applications

Xilu Wang, Xiaoping Qian

Department of Mechanical Engineering

University of Wisconsin-Madison

Madison, Wisconsin 53705

Email: xwang666@wisc.edu, qian@engr.wisc.edu

Abstract

Feature points are used to capture geometric characteristics of an object and are usually associated with certain anatomical significance or geometric meaning. The selection of feature points is a fundamental problem with various applications, for example, in shape registration, cross-parameterization, sparse shape reconstruction, parametric shape design, and dimension construction.

In the literature, feature points are usually selected on a single shape by their differential property or saliency, and the information of similar shapes in the population are not considered. Though carefully chosen feature points can represent the corresponding shape well, the variations among different shapes within the population are overlooked.

In this paper, through statistical shape modeling, we evaluate the feature points by the amount of variance they capture of the shape population, which leads to an algorithm that sequentially selects and ranks the feature points. In this way, the selected feature points explicitly incorporate the population information of the shapes. Then, we demonstrate how the proposed feature point selection approach can be integrated in the applications of sparse shape reconstruction, construction of new dimensions and shape classification through sparse measurements.

The numerical examples have validated the effectiveness and efficiency of the proposed approach.

Keywords: statistical shape modeling, feature point selection, shape variance, shape reconstruction, dimension construction

1 INTRODUCTION

Feature points are used to capture geometric characteristics of an object and are usually associated with certain anatomical significance or geometric meaning. For example, the left and right lateral malleolus points on the human body model in the CAESAR project [1] are among the anatomical feature points. The high curvature points and the extremity points are often used as geometric feature points. In [2], the heel point is defined as "the vertex having the smallest x-coordinate value".

The selection of feature points is a fundamental problem in computer graphics [3] and in CAD based custom data [4, 5] with various applications. For example, feature points are used as landmarks to guide the deformation in shape registration [6, 7, 8]. In motion tracking and 3D animation, feature points are used as marker points based on which the 3D shape is reconstructed [9, 10]. In parametric shape design, the selected feature points are used to generate semantic features [4, 5] and are used as reference points for constructing meaningful sizing dimensions[2, 11]. The selection of feature points has many more applications, including shape approximation [12] where a shape is approximated by a few points that respecting the key features, mesh segmentation [13] where each computed segment represents at least one feature point, and cross-parameterization [14, 15] where the user defined vertices for correspondence are usually selected among meaningful feature points.

In the literature, feature point is selected on a single shape by its differential property or the saliency. For example, in [6] the feature points are automatically calculated on a shape by scale saliency [16]. In [17] a center-surround operator on Gaussian-weighted mean curvatures is used to calculate the saliency map on the shape. In [13], the vertices on the convex hull of the multi-dimensional scaling (MDS) transform of the 3D mesh are selected as the feature points. In [9, 4] the landmarks on human body models were chosen by the anthropometry. In [7] 14 feature points are chosen from among local protrusion points, high-curvature points, and anatomically meaningful points.

Being carefully designed, feature points selected by the above approaches can represent the corresponding shape well. However, the population information of similar shapes are not considered and the variations among different shapes in the population are overlooked. Often, capturing the shape variations in the population is important, especially in sparse shape reconstruction and parametric shape design.

Shape reconstruction from sparse data is popular in motion tracking [9], shape completion and animation [18]. The inputs are the coordinates of the

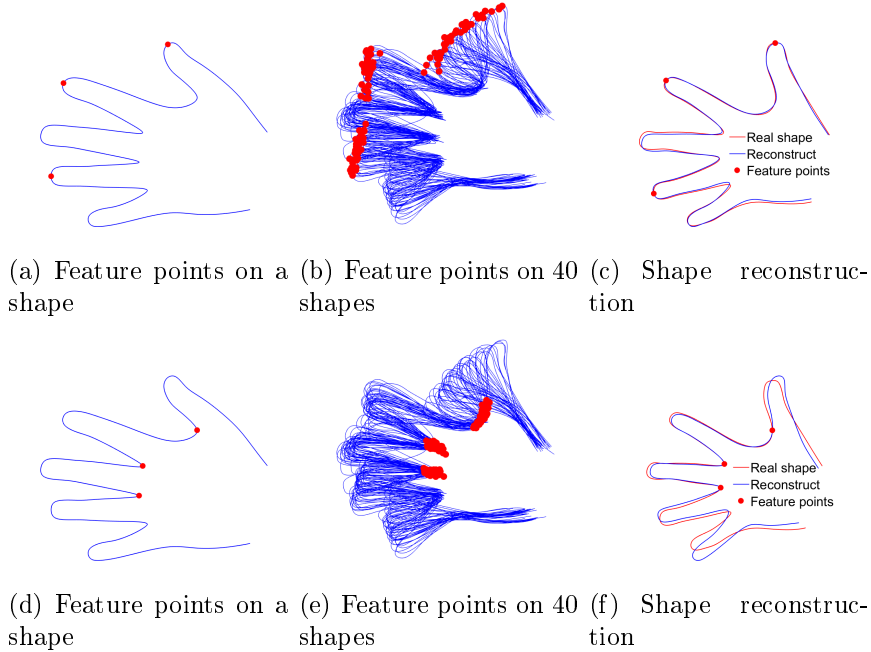


Figure 1: The effects of different feature points on sparse shape reconstruction: (a) feature points on the finger tips; (c) the variations captured by the feature points over the shape population; (c) shape reconstruction based on the feature points on the finger tips by regularized linear regression; (d) feature points on the finger valleys; (e) the variations captured by the feature points over the shape population; (f) shape reconstruction based on the feature points on the finger valleys by regularized linear regression.

feature points (sparse markers), and the output is the reconstructed shape. The mapping from feature points to a complete shape is learned by the regression analysis of the shape examples in the training set on the coordinates of the feature points [10]. If there exist variations in the population that are not captured by the feature points, then no matter how sophisticated the regression method is, the reconstructed shape would be very different from the real shape, since a part of the population information is missing.

Figure 1 shows the effects of different feature points on sparse shape reconstruction. The feature points in the top row are located at the tips of the fingers, the feature points in the bottom row are located at the valleys of the fingers. From the perspective of saliency, both of them are prominent points at high curvature areas. However, as could be seen in Figure 1(b) and 1(e), the feature points in the top row have captured the swings of the fingers while the feature points in the bottom row have not. Since swings of fingers

are the major variations in the population (compared to size and local shape changes), failing to capture them would lead to major loss of the population information. As shown in Figure 1(c) and 1(e), the shape reconstructed by the feature points in the top row is closer to the real shape than that of the bottom row.

Similarly for parametric shape design, where the inputs are sizing dimensions, the output is the synthesized shape. The mapping from sizing dimensions to a complete shape is learned by the regression analysis of the shape examples in the training set on the measured sizing dimensions [5, 4]. The obtained parametric shape model can then be used in, for example, mass-customization of foot wear [2] and personalized item design (eyeglass) [11]. As pointed out in [11], there is no standardized method to determine what suitable dimensions are and how to choose them. In [2], 24-foot dimensions (including heel length and midfoot width) are manually chosen among the lengths and angles constructed from 14 geometric feature points. In [11], 12 dimensions that are related to facial anatomy are chosen by referring to the anatomical landmarks. Since capturing population information is helpful for shape reconstruction and synthesis, we hypothesize that the chosen sizing dimensions must capture the shape variations in the training set.

In the foregoing, for the purposes of shape reconstruction and synthesis it is desirable to have the chosen dimensions capture all the major variations in the shape population. There also exist applications that need the dimensions to capture specific variations in the population. Shape classification is among such applications. The ability of rapid shape classification is critical in clinic settings. For example, it can help diagnose healthy and unhealthy anatomical structures [19] and study the effects of surgeries [20]. It is ideal to have complete 3D shapes for classification. However, due to the tedious and error-prone process [5] of obtaining neat 3D shape models from images and scanned point clouds, its applications have been limited. Since the abnormality in unhealthy and post-surgical structures are often related to some particular shape variations, it would be helpful to have a few sizing dimensions that are tightly correlated to such shape variations.

In this paper, statistical shape modeling (SSM) [21, 22] is used to learn the modes of shape variations within a population. The total variance is used to measure the amount of variations in the shape population, which is the squared sums of the projections of the shapes along the variation modes. Then, a metric is developed to quantify the amount of variance in the shape population captured by the feature points. The set of feature points that captures the highest amount of variance in the population is considered the best and is selected. Based on the selected feature points, a large pool of sizing dimensions are automatically constructed by combinatorially measuring

the distances and angles composed by the feature points. Then, depending on the applications, a subset of dimensions are selected from the pool by either maximizing the variance captured of the total population or of some particular variation modes.

The selected feature points and dimensions are compared with the ones chosen by expert. In this paper, the expert system is not referring to any specific expert, it represents the knowledge of groups of people. For example, the 67 landmarks on the human body model are chosen by the experts working on the Cesar project [1]. The landmarks are either anatomical or geometrical meaningful points that are agreed in common by the community. Similarly, the dimensions for measuring the human body shape (height, waist, breadth girth and the height of the crotch) are evaluated by the public over a long time.

The remainder of this paper is organized as follows. Section 2 briefly overviews the proposed approach. Section 3 introduces the statistical shape modeling. Section 4 demonstrates how to quantify the amount of variance in the shape population captured by the feature points and develops the algorithm for feature point selection. Section 5 illustrates how to incorporate the feature point selection approach in the applications of sparse shape reconstruction, construction of new dimensions, and shape classification by sparse measurements. Section 6 presents and analyzes the numerical results. This paper is concluded in Section 7.

2 Method overview

The proposed feature point selection approach takes two steps as shown in Figure 2: 1) statistical shape modeling to learn the shape variations in the population; 2) selecting the feature points by the amount of variance they capture of the shape population.

Given the training shapes, firstly, statistical shape modeling [21, 22] is conducted to learn the mean shape $\bar{\mathbf{S}}$ and the modes of shape variations $\Psi = [\psi_1, \psi_2, \dots, \psi_{n_s-1}]$ of the population, where n_s is the number of training shapes. The modes of shape variations span a linear shape space. Since we only have n_s number of training shapes, the shape space spanned by them is at most $n_s - 1$ dimensional. The mean shape and the variation modes span a linear shape space, any instance in the shape space can be represented as the linear combination of the mean shape and the variation modes as shown in Figure 2. The weights $\mathbf{w} = [w_1, w_2, \dots, w_{n_s-1}]^T$ of the variation modes are called the shape parameters, whose probability distribution $p(\mathbf{w})$ is learned from statistical shape modeling of the shape population. Since the variation

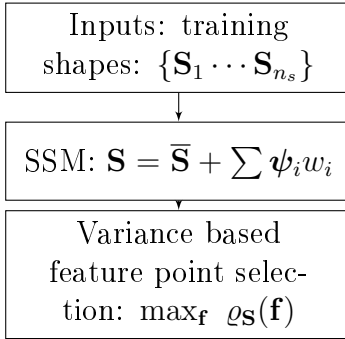


Figure 2: Total variance based feature points selection.

modes are unit vectors, the total variance of the shape population equals the total variance of the shape parameters $\text{var}(\mathbf{w})_{p(\mathbf{w})}$. The foregoing notation means the variance of \mathbf{w} under the distribution of $p(\mathbf{w})$.

Then, given the vector of feature points $\mathbf{f} = \{\mathbf{v}_{i_1} \dots \mathbf{v}_{i_{n_f}}\}$, where n_f is the total number of feature points, the conditional probability distribution of the shape parameters $p(\mathbf{w}|\mathbf{f})$ is calculated, the corresponding conditional variance $\text{var}(\mathbf{w})_{p(\mathbf{w}|\mathbf{f})}$ is obtained. The amount of variance of the shape parameters \mathbf{w} explained (captured) by the feature points \mathbf{f} is simply the difference between the total variance $\text{var}(\mathbf{w})_{p(\mathbf{w})}$ and the conditional variance $\text{var}(\mathbf{w})_{p(\mathbf{w}|\mathbf{f})}$ of the shape parameters. The percentage of the total variance in the shape population captured by the feature points is then:

$$\rho_{\mathbf{w}}(\mathbf{f}) = \frac{\text{var}(\mathbf{w})_{p(\mathbf{w})} - \text{var}(\mathbf{w})_{p(\mathbf{w}|\mathbf{f})}}{\text{var}(\mathbf{w})_{p(\mathbf{w})}}. \quad (1)$$

Thus, from the population perspective, the best set of feature points is the set that captures the highest percentage of the shape variance (1) in the population. This leads to a forward selection algorithm that sequentially selects and ranks the feature points.

Then, the selected feature points are incorporated in the applications of: 1) sparse shape reconstruction, 2) construction and selection of new dimensions, and 3) shape classification by sparse measurements.

3 Statistical shape modeling

Statistical shape modeling (SSM) [21, 22] is used to learn the variation modes of a shape population and the variances along the variation modes. In SSM each shape is represented by a set of labeled points and is treated as a vector

in the high dimensional space. Principal component analysis (PCA) is conducted to obtain the mean shape and the modes of shape variations. A linear shape space is spanned by the mean shape and the modes of shape variations. Through statistical shape modeling, a shape instance is parameterized in the linear shape space by a few shape parameters, the probabilistic distribution of the shapes in the linear space is modeled by the probabilistic distribution of the shape parameters. Statistical shape modeling usually contains three steps: shape registration, shape alignment, and principal component analysis.

Given the training set of n_s number of shapes $\mathcal{S} = \{\mathbf{S}_1^{raw}, \mathbf{S}_2^{raw}, \dots, \mathbf{S}_{n_s}^{raw}\}$, in order to correctly calculate the population mean and model the shape variations, accurate correspondences between the shapes must be built. Otherwise unrealistic artifacts will be incorporated into the shape variations and the obtained shape variances will be larger than the actual shape variances since variances of the artifacts are included.

The goal of shape registration is to find the correspondences between two shapes, which associate a point in one shape to a point in another shape. Some well established shape registration methods include the rigid ICP (iterative closest point) algorithm [23], the non-rigid ICP algorithm [24, 7], the free-form deformation based approach [25, 26], cross-parameterization [14, 15] and reparameterization [27, 28]. In this paper, we assume that the shape models are all complete and discard incomplete shapes in the training set. For correspondences of incomplete shapes, the method in [29] that computes partial functional correspondence between two shapes can be applied.

In this work, the deformation based approach is used for shape registration. A reference shape \mathbf{S}_{ref} is chosen from among the training shapes $\{\mathbf{S}_1^{raw}, \dots, \mathbf{S}_{n_s}^{raw}\}$ and is deformed to each training shape to find the correct shape correspondences. Ideally, the reference shape should be close to the mean shape of the population. In practice, the mean shape is unknown initially, the reference shape is chosen by avoiding the extreme cases that it is far away from most of the other shapes in the population, since large shape deformations are usually not robust [8]. The shape registration process takes three steps: firstly, the reference shape is rigidly aligned (through rotations and translations) to the training shape by the rigid ICP algorithm [23]; Then the reference shape is further deformed to the training shape through iterative free-form deformations [8, 25, 26]; Finally, the vertices of the deformed reference shape are projected onto the training shape along the directions of normal vectors. For more details of the registration process please refer to the paper [8]. Based on the obtained correspondences, the training shapes

are re-sampled by the same number of points in correspondence

$$\mathbf{S}_k = [\mathbf{v}_1^{(k)}, \dots, \mathbf{v}_{n_v}^{(k)}]^t, \quad k = 1, \dots, n_s, \quad (2)$$

where \mathbf{S}_k is the k th re-sampled training shape, n_v is the number of sampling points on each shape, n_s is the number of training shapes, and $\mathbf{v}_i^{(k)} = [x_i^{(k)}, y_i^{(k)}, z_i^{(k)}]$ are the coordinates of the i th vertex on the k th shape.

Generalized Procrustes analysis [30] is then conducted to align the registered shapes $\{\mathbf{S}_1, \dots, \mathbf{S}_{n_s}\}$ to the same coordinate frame and to eliminate the effects of translation and rotation. In the following context, training shapes $\{\mathbf{S}_1, \dots, \mathbf{S}_{n_s}\}$ will denote the "re-sampled training shapes in the same coordinate frame" without ambiguity.

Principal component analysis (PCA) is conducted for capturing shape variations and dimensional reduction. In PCA, each shape is treated as a vector in \mathbb{R}^{3n_v} by concatenating the coordinates of the points. The mean shape of the population is

$$\bar{\mathbf{S}} = \frac{1}{n_s} \sum_{k=1}^{n_s} \mathbf{S}_k, \quad (3)$$

the shape covariance matrix is

$$\Sigma = \frac{1}{n_s - 1} \Phi \Phi^T, \quad (4)$$

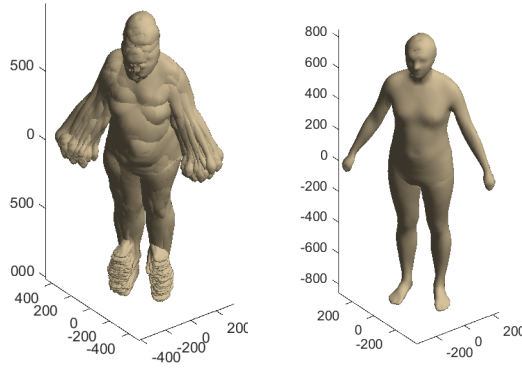
where $\Phi = [\mathbf{S}_1 - \bar{\mathbf{S}}, \dots, \mathbf{S}_{n_s} - \bar{\mathbf{S}}]$. Just as all the covariance matrices do, the shape covariance matrix Σ describes the patterns and ranges of variations from the mean $\bar{\mathbf{S}}$. Through eigen-decomposition, we have

$$\Sigma \psi_k = \lambda_k \psi_k, \quad k = 1, \dots, n_s - 1, \quad (5)$$

where $\psi_1, \dots, \psi_{n_s-1}$ are the principal components of the covariance matrix Σ , $\lambda_1, \dots, \lambda_{n_s-1}$ are the corresponding eigenvalues. The principal components capture the modes of shape variations (also called eigen-shapes). The eigenvalues are the amount of variances in those components.

Figure 3 shows the training shapes of the human body model and the corresponding mean shape. Figure 3 shows the first three eigen-shapes of the population. The first eigen-shape is related to the change in height, the second eigen-shape is related to the change in width, and the third eigen-shape is related to some local shape changes. The obtained mean shape $\bar{\mathbf{S}}$ and eigen-shapes $\psi_1, \dots, \psi_{n_s-1}$ span a linear shape space. An instance in the shape space can be represented by:

$$\mathbf{S} = \bar{\mathbf{S}} + \sum_{k=1}^{n_s-1} w_k \psi_k, \quad (6)$$



(a) Training Shapes (b) Mean shape

Figure 3: Shape population of human body: (a) training shapes in the same coordinate frame; (b) the mean shape. Unit is millimeter.

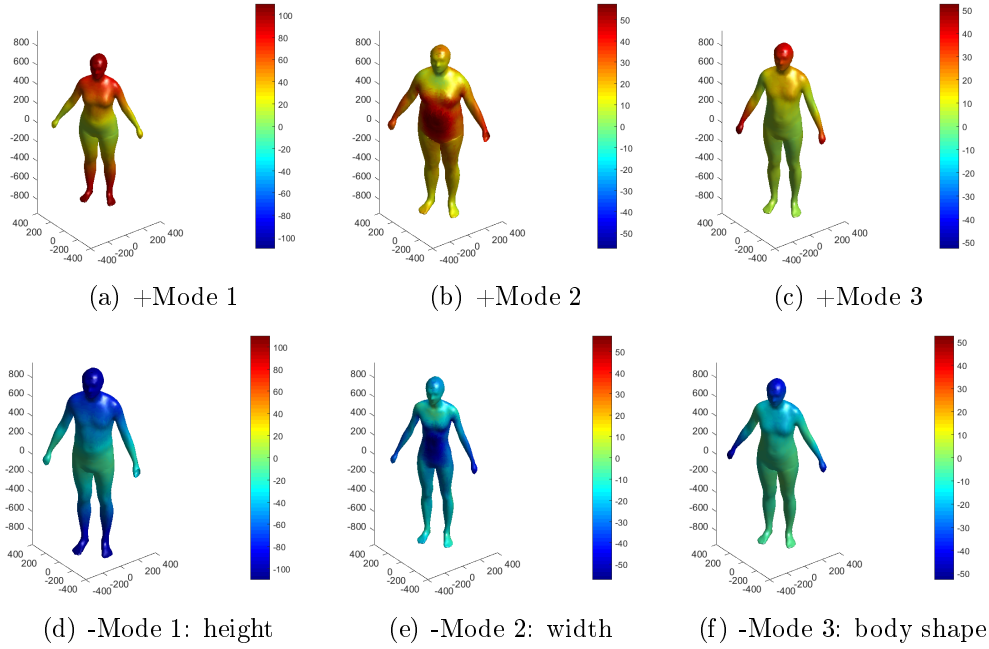


Figure 4: The first three eigen-shapes. Color shows the surface deviation from the mean shape, unit is millimeter.

where $w_1 \dots w_{n_s-1}$ are the weights on each mode and are called the shape parameters. The shape parameters uniquely determine an instance in the shape space. For a training shape \mathbf{S}_i , its shape parameters can be obtained by projecting it into the shape space:

$$w_{i,k} = (\mathbf{S}_i - \bar{\mathbf{S}})^T \boldsymbol{\psi}_k, \quad i = 1, \dots, n_s, \quad k = 1, \dots, n_s - 1, \quad (7)$$

where $w_{i,k}$ means the k th shape parameter for the i th shape.

Practically, we do not incorporate all the eigen-shapes into the model as in equation (6), for the sake of compactness and noise removal. The noises are usually come from the errors in shape retrieving processes such as image segmentation, shape reconstruction and surface rectification.

A truncated statistical shape model would be

$$\mathbf{S} = \bar{\mathbf{S}} + \sum_{k=1}^m w_k \boldsymbol{\psi}_k + \boldsymbol{\epsilon}, \quad (8)$$

where m is the number of modes chosen and can be determined, e.g. from $\sum_{k=1}^m \lambda_k / \sum_{k=1}^{n_s-1} \lambda_k \geq 99\%$, which means that the first m modes should capture more than 99% of the total shape variances in the training set, where $\boldsymbol{\epsilon} = [\epsilon_1, \dots, \epsilon_{3n_v}]^T$ is the random vector that captures the remaining shape variances in the population, and $\mathbf{w} = [w_1, w_2, \dots, w_m]^T$ is the truncated vector of shape parameters.

Assuming that the shapes are normally distributed, the probability density of the vector of the shape parameters \mathbf{w} is:

$$p(\mathbf{w}) = |2\pi\Lambda|^{-\frac{1}{2}} e^{-\frac{1}{2}\mathbf{w}^T \Lambda^{-1} \mathbf{w}}, \quad \Lambda = \text{diag}(\lambda_1, \dots, \lambda_m) \quad (9)$$

where λ_i is the i th eigenvalue of the principal component analysis, and "diag" means diagonal matrix.

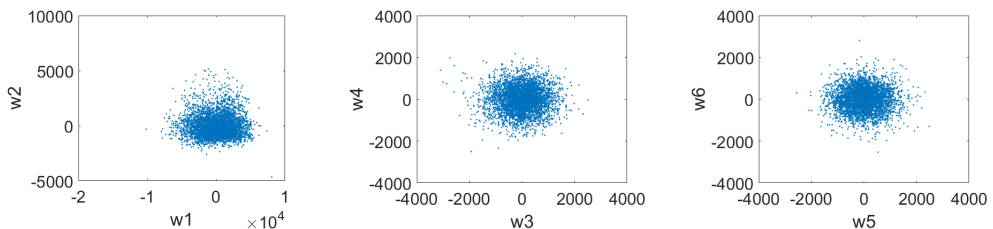


Figure 5: The distributions of the shape parameters. Unit is millimeter.

Figure 5 shows the distributions of the first six shape parameters obtained by projecting the shapes on the eigen-modes by equation (7). It can be seen

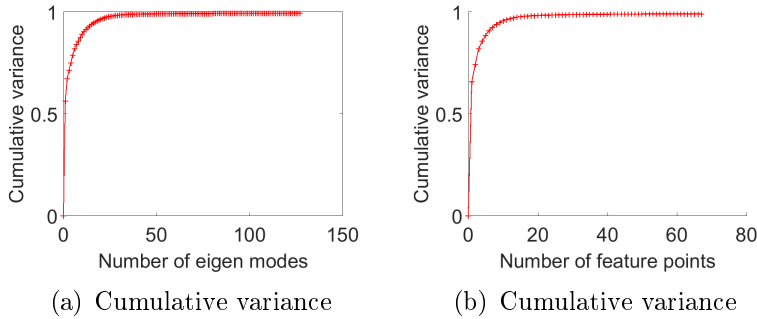


Figure 6: The percentage variance of the training shapes captured by the increasing number of (a) eigenvectors; (b) feature points.

that the shapes of the distributions are similar to discs with denser points in the center and sparser points at the outer area. Thus the normal distribution would be a good approximation to the true distribution. Figure 6 shows the cumulative variance of the shape population captured by the increasing number of eigen-modes (shape parameters).

While most researches leverage the synthesis power of the statistical shape model and focus on shape synthesis by the mean shape and the eigen-shapes, we view equations (8) and (9) as the probabilistic description of the shape space and build our method on it.

4 Feature point identification

Through statistical shape modeling, the eigen-modes of the shape population are learned and are ranked by the amount of percentage variance they capture of the shape population, as shown in Figure 6(a). Since the goal of feature point selection is to capture as much information as possible of the shape population, in this section, the feature points are selected and ranked by the amount of percentage variance they capture of the shape population, as shown in Figure 6(b).

With the statistical shape model (8), a shape in the population is parameterized by a few shape parameters $\{w_1, \dots, w_m\}$, and the major amount of variance (i.e. 99.5%) in the population is captured by the variances of the shape parameters $\{\lambda_1, \dots, \lambda_m\}$, which are the eigenvalues of the shape covariance matrix Σ . The remaining variance is captured by the residual vector ϵ in (8). Since it is not meaningful to capture the variance in the residual vector, the selected feature points are targeted to capture as much variance in the shape parameters as possible.

The inputs of the feature point selection are the statistical shape model and the number of points to be selected: n_f . The outputs are the vertex indices of the selected feature points $\mathbb{I} = \{i_1, \dots, i_{n_f}\} \subset \{1, \dots, n_v\}$, where n_v is the total number of vertices. The feature points on the shape vectors can then be sampled by the indices, for example, the vectors of feature points on the n_s number of training shapes are:

$$\mathbf{F} = [\mathbf{f}_1, \mathbf{f}_2, \dots, \mathbf{f}_{n_s}], \quad (10)$$

where $\mathbf{f}_k = [\mathbf{v}_{i_1}^{(k)}, \mathbf{v}_{i_2}^{(k)}, \dots, \mathbf{v}_{i_{n_f}}^{(k)}]^T$ is the vector of feature points sampled on the k th training shape, which is abbreviated as the feature vector in the latter context.

Truncating the rows of equation (8) according to the indices of the feature points, we have:

$$\mathbf{f} = \bar{\mathbf{S}}_f + \Psi_f \mathbf{w} + \boldsymbol{\epsilon}_f, \quad (11)$$

where \mathbf{f} is the corresponding rows of the shape vector \mathbf{S} , $\bar{\mathbf{S}}_f$ is the corresponding rows of the mean shape $\bar{\mathbf{S}}$, Ψ_f is the corresponding rows of the matrix of eigenvectors $\Psi = [\psi_1 \dots \psi_m]$, and $\boldsymbol{\epsilon}_f$ is the corresponding rows of the residual vector $\boldsymbol{\epsilon}$.

The covariance matrix of the shape parameters are known from the principal component analysis $\Lambda = \text{diag}(\lambda_1, \dots, \lambda_m)$. Assuming that the elements $\epsilon_i, i = 1, \dots, 3n_v$ of the residual vector $\boldsymbol{\epsilon}$ are independent and identically distributed, the covariance matrix of the residual vector is diagonal and can be modeled by

$$\text{Cov}(\boldsymbol{\epsilon}) = \epsilon \mathbf{I}, \quad \text{Cov}(\boldsymbol{\epsilon}_f) = \epsilon \mathbf{I}_f$$

where \mathbf{I} is the identity matrix and \mathbf{I}_f is the corresponding truncation, ϵ is the variance of each element ϵ_i in the residual vector and is modeled by

$$\epsilon = \sum_{k=m+1}^{n_s-1} \lambda_k / 3n_v + c, \quad (12)$$

where $\sum_{k=m+1}^{n_s-1} \lambda_k / 3n_v$ captures the remaining variances in the discarded eigenmodes and c accounts for the variances brought by the errors in the shape retrieving process such as laser scanning or image segmentation.

Since the covariance matrices of the shape parameters and the residual vector are now known, the covariance matrix of the feature vector \mathbf{f} and

the covariances between the feature vector and the shape parameters can be calculate from equation (11) as

$$\text{Cov}(\mathbf{f}, \mathbf{f}) = \Psi_f \Lambda \Psi_f^T + \epsilon \mathbf{I}, \quad \text{Cov}(\mathbf{f}, \mathbf{w}) = \Psi_f \Lambda, \quad \text{Cov}(\mathbf{w}, \mathbf{f}) = \Lambda \Psi_f^T, \quad (13)$$

where Cov represents the covariance matrix.

In statistical shape modeling, it is assumed that the shape parameters are normally distributed. Since equation (11) represents a linear relationship between \mathbf{f} and \mathbf{w} , so their joint distribution is also normal distribution:

$$p(\mathbf{f}, \mathbf{w}) \sim N\left(\begin{bmatrix} \bar{\mathbf{S}}_f \\ 0 \end{bmatrix}, \begin{bmatrix} \Psi_f \Lambda \Psi_f^T + \epsilon \mathbf{I} & \Psi_f \Lambda \\ \Lambda \Psi_f^T & \Lambda \end{bmatrix}\right), \quad (14)$$

where $N(\cdot, \cdot)$ stands for the normal distribution with the first parameter its mean and the second parameter its covariance matrix. The conditional distribution of the shape parameters \mathbf{w} given the feature vector \mathbf{f} is:

$$p(\mathbf{w}|\mathbf{f}) \sim N\left(\Lambda \Psi_f^T (\Psi_f \Lambda \Psi_f^T + \epsilon \mathbf{I})^{-1} (\mathbf{f} - \bar{\mathbf{S}}_f), \Lambda - \Lambda \Psi_f^T (\Psi_f \Lambda \Psi_f^T + \epsilon \mathbf{I})^{-1} \Psi_f \Lambda\right). \quad (15)$$

The first term inside $N(\cdot, \cdot)$ is the conditional mean, and the second term is the conditional covariance matrix. Originally, the shape parameters are distributed in a relatively larger area shaped by its covariance matrix Λ . Given the observation of the feature points \mathbf{f} , the shape becomes less free since it has to conform with the observed feature points. So the shape parameters are also less free and are distributed in a smaller area shaped by the conditional covariance matrix $\Lambda - \Lambda \Psi_f^T (\Psi_f \Lambda \Psi_f^T + \epsilon \mathbf{I})^{-1} \Psi_f \Lambda$, which tells us the remaining covariance structure of the shape parameters given the observation of the feature points. The remaining variance in the shape parameters is $\text{trace}(\Lambda - \Lambda \Psi_f^T (\Psi_f \Lambda \Psi_f^T + \epsilon \mathbf{I})^{-1} \Psi_f \Lambda)$, thus the total amount of variance in the shape parameters explained by the feature points is

$$r_{\mathbf{w}}(\mathbf{f}) = \text{trace}(\Lambda) - \text{trace}(\Lambda - \Lambda \Psi_f^T (\Psi_f \Lambda \Psi_f^T + \epsilon \mathbf{I})^{-1} \Psi_f \Lambda) \quad (16)$$

$$= \text{trace}(\Lambda \Psi_f^T (\Psi_f \Lambda \Psi_f^T + \epsilon \mathbf{I})^{-1} \Psi_f \Lambda), \quad (17)$$

and the percentage of the variance in the training shapes explained by the feature points is

$$\varrho_{\mathbf{S}}(\mathbf{f}) = \text{trace}(\Lambda \Psi_f^T (\Psi_f \Lambda \Psi_f^T + \epsilon \mathbf{I})^{-1} \Psi_f \Lambda) / \sum_{k=1}^{n_s-1} \lambda_k. \quad (18)$$

By equation (18), we have Definition 1 for the selection of feature points.

Definition 1: The most important feature points on the shapes are the ones that capture the highest percentage of the variance of the shape population.

By Definition 1, the optimization formula for feature point selection is:

$$\max_{\{i_1 \dots i_{n_f}\} \subset \{1 \dots n_v\}} \varrho_S(\mathbf{f}). \quad (19)$$

Assuming that the set of training shapes well represent the underlying shape population and the subject-shapes that will be encountered in future follow the same distribution $p(\mathbf{f}, \mathbf{w})$, we have the expectation of the squared error of shape reconstructions by the chosen feature points is:

$$\begin{aligned} E^{se} &= \int (\mathbf{w}_{test} - \tilde{\mathbf{w}})^T (\mathbf{w}_{test} - \tilde{\mathbf{w}}) p(\mathbf{w}_{test} | \mathbf{f}) \\ &= \text{trace}(\Lambda - \Lambda \Psi_f^T (\Psi_f \Lambda \Psi_f^T + \epsilon \mathbf{I})^{-1} \Psi_f \Lambda), \end{aligned} \quad (20)$$

where $\tilde{\mathbf{w}} = \Lambda \Psi_f^T (\Psi_f \Lambda \Psi_f^T + \epsilon \mathbf{I})^{-1} (\mathbf{f} - \bar{\mathbf{S}}_f)$ is the conditional mean in (15) and is used to estimate the shape parameters from the positions of the feature points. If the feature points are selected according to (19), then E^{se} is minimized.

However, the optimization problem in (19) is *NP* hard [31] whose global optimal can only be achieved by exhaustive search, which is very time consuming. For example, selecting 30 feature points from the human body shape with 6000 vertices will evaluate equation (18) for $C_{6000}^{30} = 7.75e + 80$ times, which is computationally prohibitive. Instead of optimizing globally, here a forward selection algorithm is developed for two reasons: 1) it efficiently finds a suboptimal solution that is good enough; 2) it gives a ranking of the selected feature points that tells which points are more important and which are less.

Algorithm 1 Forward selection for feature point identification

1. Initialize the set of vertex indices for the feature points to be empty: $\mathbb{I} = \{\}$, and the number of feature points $n_f = 0$.
 2. Update $n_f = n_f + 1$ and $\mathbb{I} = \mathbb{I} \cup \{i\}$ if $i \in \{1, \dots, n_v\}$ maximizes $\varrho_S(\mathbf{v}_{\mathbb{I} \cup \{i\}})$, where $\mathbf{v}_{\mathbb{I} \cup \{i\}} = [\mathbf{v}_{\mathbb{I}}^T, \mathbf{v}_i]^T$.
 3. Exit if $\varrho_S(\mathbf{v}_{\mathbb{I}}) < \varrho^*$ (e.g. $\varrho^* = 0.98$); else go to step 2.
-

It should be noted that in each step in Algorithm 1, the best point is found by exhaustively searching all the candidate points. For example, the first point is found by evaluating equation (18) with respect to all the vertices. The time complexity of Algorithm 1 is $O(n_v n_f)$, where n_v is the number of

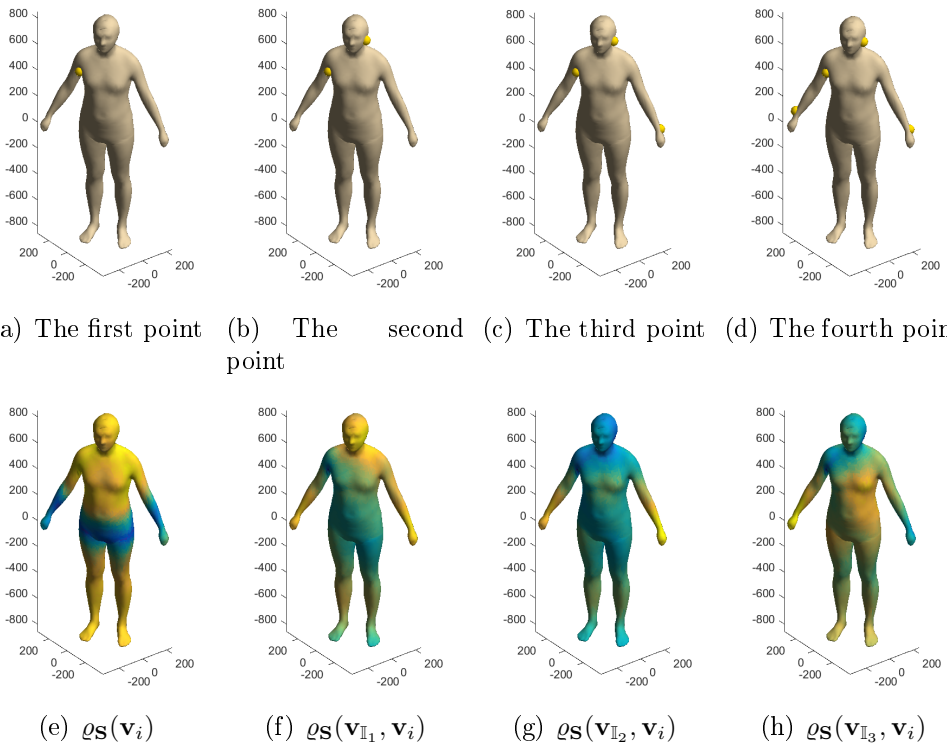


Figure 7: Feature points (yellow balls) on the human body model selected by Algorithm 1. The color shows the percentage variance $\varrho_{\mathbf{S}}(\mathbf{v}_{\mathbb{I}}, \mathbf{v}_i)$ captured by moving the corresponding feature point on the shape surface. The warmest color corresponds to the highest percentage of variance. Unit is millimeter.

vertices and n_f is the number of feature points, which is much smaller than the combinatorial number $C_{n_v}^{n_f}$.

Similar greedy algorithms have been applied in [32, 33] to select the most powerful feature points for pairwise shape registration by iterative closest point algorithm. For example in [33] a two-phase feature point selection algorithm is developed. In the forward selection, at each step the point that has the maximum projection onto the first eigenvector is selected. In the backward elimination, the points that are least significant in the current eigenvectors are removed. The forward selection and backward elimination are nested so to avoid bad local minimums.

Figure 7 shows the first four feature points selected by Algorithm 1. The color shows the percentage variance $\varrho_{\mathbf{S}}(\mathbf{v}_{\mathbb{I}}, \mathbf{v}_i)$ captured by moving the corresponding feature point on the surface of the shape. The warmest color corresponds to the highest percentage of variance, and is where the next feature point is put.

5 Applications

In this section, we demonstrate how to incorporate the feature point identification approach in the below applications: 1) sparse shape reconstruction; 2) dimensions construction and selection; 3) shape classification by sparse measurements.

5.1 Sparse shape reconstruction

The feature points are selected by maximizing the amount of variance they capture of the shape population, which makes them powerful for being the marker points in sparse shape reconstruction.

The shape reconstruction is based on the statistical shape model and takes two steps:

1) Estimate the corresponding shape parameters $\mathbf{w} = [w_1, w_2, \dots, w_m]^T$ by the coordinates of the observed feature points

$$\tilde{\mathbf{w}} = \Lambda \Psi_f^T (\Psi_f \Lambda \Psi_f^T + \epsilon \mathbf{I})^{-1} (\mathbf{f} - \bar{\mathbf{S}}_f), \quad (21)$$

note that $\tilde{\mathbf{w}}$ is the conditional mean in (15). Equation (21) represents a linear relationship between the feature points and the shape parameters and could be viewed as a type of regularized linear regression.

2) Reconstruct the shape by the estimated shape parameters $\tilde{\mathbf{S}} = \bar{\mathbf{S}} + \Psi \tilde{\mathbf{w}}$.

Through statistical shape modeling, the probabilistic distribution $p(\mathbf{w})$ of the shape parameters is obtained as in (9). Without any other information, the maximum likelihood estimation of the shape parameters will be $\mathbf{w} = \mathbf{0}$, which is just the mean shape. Given the information of the feature vector \mathbf{f} , the conditional distribution $p(\mathbf{w}|\mathbf{f})$ of the shape parameters is obtained as in equation (15). The maximum likelihood estimation of \mathbf{w} is then the corresponding conditional expectation as in equation (21).

5.2 Dimension construction and selection

As pointed out in [11], there is no standardized method to determine what the suitable dimensions are and how to choose them for the parametric shape design. In their study, twelve dimensions that are related to facial anatomy are chosen. In [7], 24 dimensions were manually constructed from the 14 geometrical feature points chosen by experts in anthropometry. Here, a way to automatically construct and select sizing dimensions is given. It takes two steps: firstly, a dimension pool that contains a large number of dimensions is automatically constructed. Secondly, a subset of the dimensions in the pool

is selected and ranked by the amount of variance they capture of the shape population.

The dimension pool is composed of lengths and angles obtained by measuring the feature points combinatorially. For example, given the feature points $\mathbf{v}_{i_1}, \mathbf{v}_{i_2}, \dots, \mathbf{v}_{i_{n_f}}$, $C_{n_f}^2 = n_f(n_f - 1)/2$ number of length dimensions are constructed:

$$\{l_1, l_2, \dots, l_{n_f(n_f-1)/2}\}. \quad (22)$$

Similarly, $3C_{n_f}^3 = n_f(n_f - 1)(n_f - 2)/2$ number of angle dimensions are constructed by each time choosing three feature points and measuring the angles of the composed triangle:

$$\{\theta_1, \theta_2, \dots, \theta_{n_f(n_f-1)(n_f-2)/2}\}. \quad (23)$$

Combined with the list of traditional measurements [1], a big pool of dimensions is constructed:

$$\mathbb{P} = \{l_1, l_2, \dots, l_N\}. \quad (24)$$

A subset of dimensions $\mathbf{L} = [l_{j_1}, l_{j_2}, l_{j_{n_j}}]$ is selected from the pool \mathbb{P} by maximizing the variance they capture of the shape population.

It is helpful to exploit the existing human knowledge when possible. In such cases the dimensions that are automatically derived and constructed from our algorithm act as a complementary for the traditional measurements and are aimed to capture the shape variations that are not captured by the traditional measurements.

It is worth noting that \mathbb{P} usually contains hundreds or even thousands of dimensions (e.g. $C_{12}^2 = 66, 3C_{12}^3 = 660$). Some of the dimensions in \mathbb{P} may be correlated or even dependent on each other. However, the goal of dimension construction is to create enough number of candidates for the dimension selection. It doesn't matter whether the dimensions in \mathbb{P} are dependent or not, since the selected dimensions will be as independent as possible. Any dimension that is dependent on the dimensions in \mathbf{L} will not be selected since it has no contribution to capturing the population variance.

In order to compute the amount of variance of the shape population captured by the selected dimensions, the joint probability $p(\mathbf{w}, \mathbf{L})$ of the shape parameters \mathbf{w} and the sizing dimensions \mathbf{L} is learned from the training shapes. The covariance matrix Λ of the shape parameters is already known by statistical shape modeling. The covariance matrix Σ_l of the selected dimensions \mathbf{L} is obtained by measuring on the training shapes:

$$\Sigma_l = \sum_{k=1}^{n_s} (\mathbf{L}_k - \bar{\mathbf{L}})(\mathbf{L}_k - \bar{\mathbf{L}})^T / (n_s - 1), \quad (25)$$

where \mathbf{L}_k are the measurements on the k th training shape, and $\bar{\mathbf{L}} = \sum_{k=1}^{n_s} \mathbf{L}_k / n_s$ is the mean dimension vector over the training shapes. The covariance matrix between the shape parameters and the sizing dimensions is obtained by:

$$\Sigma_{lw} = \sum_{k=1}^{n_s} (\mathbf{L}_k - \bar{\mathbf{L}}) \mathbf{w}_k^T / (n_s - 1), \quad (26)$$

where \mathbf{w}_k is the vector of shape parameters for the k th training shape. Under the assumption of normal distribution, we have the joint probability

$$p(\mathbf{L}, \mathbf{w}) \sim N\left(\begin{pmatrix} \bar{\mathbf{L}} \\ 0 \end{pmatrix}, \begin{pmatrix} \Sigma_l & \Sigma_{lw} \\ \Sigma_{wl} & \Lambda \end{pmatrix}\right), \quad (27)$$

where $N(\cdot, \cdot)$ stands for the normal distribution. The corresponding conditional probability distribution is:

$$p(\mathbf{w}|\mathbf{L}) \sim N(\Sigma_{wl}\Sigma_l^{-1}(\mathbf{L} - \bar{\mathbf{L}}), \Lambda - \Sigma_{wl}\Sigma_l^{-1}\Sigma_{lw}), \quad (28)$$

where the first term inside $N(\cdot, \cdot)$ is the conditional mean, and the second term is the conditional covariance. The variance in the shape parameters captured by the selected dimensions is:

$$\begin{aligned} \text{var}(\mathbf{w})_{p(\mathbf{w})} - \text{var}(\mathbf{w})_{p(\mathbf{w}|\mathbf{L})} &= \text{trace}(\Lambda) - \text{trace}(\Lambda - \Sigma_{wl}\Sigma_l^{-1}\Sigma_{lw}) \\ &= \text{trace}(\Sigma_{wl}\Sigma_l^{-1}\Sigma_{lw}) \end{aligned} \quad (29)$$

The percentage of the variance in the training shapes explained by the selected dimensions is:

$$\varrho_{\mathbf{s}}(\mathbf{L}) = \text{trace}(\Sigma_{wl}\Sigma_l^{-1}\Sigma_{lw}) / \sum_{k=1}^{n_s-1} \lambda_k. \quad (30)$$

Based on the foregoing deducing, we have Definition 2 for the dimension selection.

Definition 2: the best set $\mathbf{L} = [l_{j_1}, l_{j_2}, \dots, l_{j_{n_l}}] \subset \mathbb{P}$ of dimensions is the one that captures the highest percentage of the variance of the shape population:

$$\max_{\{l_{j_1} \dots l_{j_{n_l}}\} \subset \mathbb{P}} \varrho_{\mathbf{s}}(\mathbf{L}). \quad (31)$$

Assuming that the set of training shapes well represent the underlying shape population, the shape parameters and sizing dimensions are normally

distributed, and the subject-shapes that will be encountered in future follow the same distribution $p(\mathbf{L}, \mathbf{w})$, we have the expectation of the squared error of parametric shape synthesis by the selected dimensions is:

$$\begin{aligned} E^{se} &= \int (\mathbf{w}_{test} - \tilde{\mathbf{w}})^T (\mathbf{w}_{test} - \tilde{\mathbf{w}}) p(\mathbf{w}_{test} | \mathbf{L}) \\ &= \text{trace}(\Lambda - \Sigma_{wl} \Sigma_l^{-1} \Sigma_{lw}), \end{aligned} \quad (32)$$

where $\tilde{\mathbf{w}} = \Sigma_{wl} \Sigma_l^{-1} (\mathbf{L} - \bar{\mathbf{L}})$ is the conditional mean in (28) and is used to synthesize the shape parameters from the sizing dimensions. If the dimensions are selected according to (31), then E^{se} is minimized.

Similar as in formula (19), the optimization problem in (31) is *NP* hard [31]. A forward selection algorithm is developed for 1) efficient dimension selection, and 2) ranking the selected dimensions.

Algorithm 2 Forward selection for dimension identification

1. Initialize the set of dimensions to be empty: $\mathbf{L} = \{\}$, and the number of dimensions $n_l = 0$.
 2. Update $n_l = n_l + 1$ and $\mathbf{L} = [\mathbf{L}^T, l_j]^T$ if $l_j \in \{l_1, \dots, l_N\}$ maximizes $\varrho_s([\mathbf{L}^T, l_j]^T)$.
 3. Exit if $\varrho_s(\mathbf{L}) < \varrho^*$ (e.g. $\varrho^* = 0.98$); else go to step 2.
-

The selected dimensions can be applied in the parametric shape design [4], the mass-customization [7] and the personalized item design [11], since a faithful 3D shape model of the given subject can be efficiently synthesized by the conditional mean in (28).

5.3 Shape classification by key dimensions

Shape classification is of critical importance in clinics. It can help diagnosis healthy and unhealthy anatomical structures [19] and study the effects of surgeries [20]. It is ideal to have complete shape models for classification and comparing. However, due to the tedious and error-prone process [5] of obtaining neat shape models from images and scanned point clouds, its applications have been limited.

In this section an approach is proposed to construct and select dimensions that can effectively distinguish two different groups of shapes, it takes two steps:

1) Identify the shape parameters $\hat{\mathbf{w}} = [w_{i_1}, \dots, w_{i_d}]^T \subset [w_1, \dots, w_m]$ that are related to group differences. Since the shape parameters are uncorrelated to each other due to principal component analysis, the student-t-test is conducted for each shape parameter separately to decide whether that shape parameter shows differences across the two groups.

2) The dimensions are selected to capture the variances in the selected shape parameters $\hat{\mathbf{w}} = [w_{i_1}, \dots, w_{i_d}]^T$:

$$\max_{\{l_{j_1} \dots l_{j_{n_l}}\} \subset \mathbb{P}} \varrho_{\hat{\mathbf{w}}}(\mathbf{L}) = \text{trace}(\Sigma_{\hat{w}l}\Sigma_l^{-1}\Sigma_{l\hat{w}})/\sum_{k=1}^d \lambda_{i_k}. \quad (33)$$

6 Numerical examples

The numerical examples are used to test the proposed feature point identification approach and to demonstrate its applications in sparse shape reconstruction, construction of new dimensions and shape classification by sparse measurements.

6.1 The Caesar human body models

The Caesar human body database [1] is used to demonstrate the feature point identification and its applications in sparse shape reconstruction and construction of new dimensions. The human body shape models are represented by boundary triangulations, and the 4308 fitted meshes $\{\mathbf{S}_1, \mathbf{S}_2, \dots, \mathbf{S}_{4308}\}$ in [34] are used in this paper. The meshes in [34] are already sampled by the same number of points in correspondence thus non-rigid shape registration is not needed as a pre-processing step. Only the last two steps of statistical shape modeling are performed (general Procrustes analysis and principal component analysis). Among the 4308 shape models, 4092 shapes are used as the training shapes to learn the statistical shape model, select the feature points, and construct new dimensions, 216 shapes are used as the testing shapes for validation. Ideally, to eliminate the sampling bias, the training shapes and testing shapes should be sampled randomly from the database, however, for the repeatability of the results, the testing shapes are sampled by an interval of 20:

$$\mathbb{S}^{test} = \{\mathbf{S}_1, \mathbf{S}_{21}, \mathbf{S}_{41}, \dots, \mathbf{S}_{4301}\}. \quad (34)$$

The remaining shapes are used as the training shapes:

$$\mathbb{S}^{train} = \{\mathbf{S}_2, \mathbf{S}_3, \dots, \mathbf{S}_{20}, \mathbf{S}_{22}, \mathbf{S}_{23}, \dots, \mathbf{S}_{40}, \dots, \mathbf{S}_{4308}\}. \quad (35)$$

6.1.1 Feature point identification

At the previous section in Figure 7 we show the first four feature points selected from the 6449 vertices by Algorithm 1. Figure 8 shows more intermediate results as Algorithm 1 goes from $n_f = 5$ to $n_f = 30$, where n_f is the number of feature points. The top and bottom rows in Figure 8 show the front and back views of the human body model. The corresponding statistical shape model is as shown in Section 2.

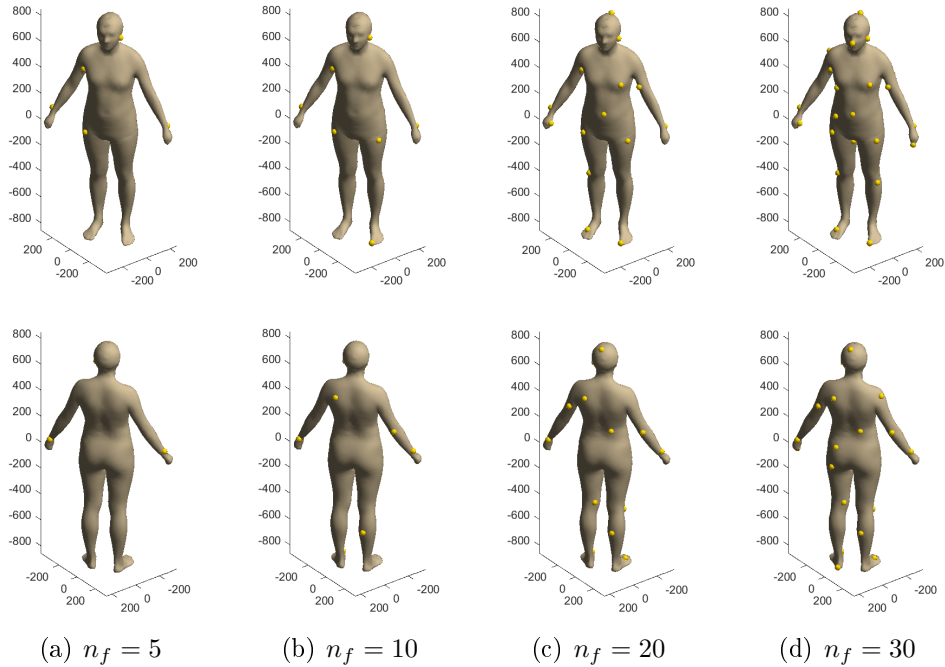


Figure 8: The selected feature points (yellow sphere) on the human body model: (a) 5 feature points; (b) 10 feature points; (c) 20 feature points; (d) 30 feature points. The upper and lower rows show the front and back views. Unit is millimeter.

As shown in Figure 7 and Figure 8(a), the first point is placed at the armpit, whose position is highly correlated with the first two variation modes (height and width); the second point is placed near the ear (the real ear is missing due to smoothing), which captures the variations above the shoulder; the third and fourth points are placed at the wrists, which capture the variations in the arm length and poses, the fifth point is at the waist, which tell us something about the lower body (i.e. waist height and width).

Checking the other sub-figures in Figure 8, it can be seen that the selected feature points distribute evenly on the human body and many of them are

at the anatomically meaningful places. For example, the point at the belly button, the points at the toes and heels, and the points at the joints (knee joints, arm joints), which shows the reasonability of Algorithm 1.

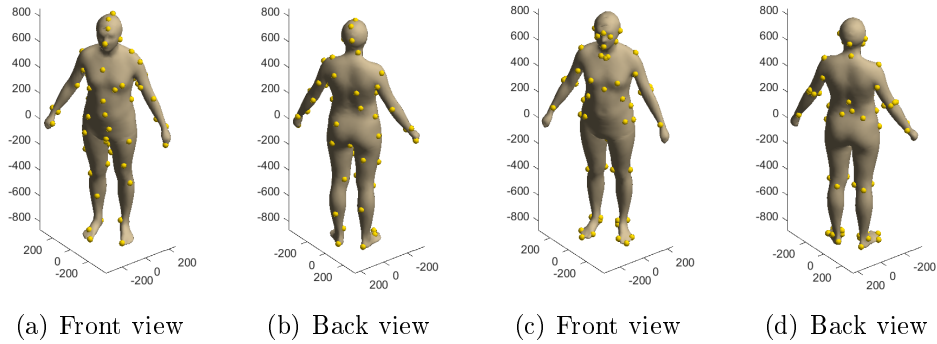


Figure 9: The 67 feature points selected by (a) and (b) Algorithm 1, (c) and (d) well defined anatomical landmarks from CAESAR. Unit is millimeter.

Figure 9 compares the 67 feature points selected by Algorithm 1 and the 67 well defined anatomical landmarks in CAESAR project [1]. It can be seen that the feature points selected by Algorithm 1 are distributed more evenly. For example, the anatomical landmarks from CAESAR database do not have points on the hip, however the shape variation of hip is non-negligible across the population.

In the foregoing, the feature points are selected from all the 6449 vertices on the human body model by Algorithm 1. However, the precise positions of some of the selected feature points are hard to locate (e.g. the points in the vast middle area of the belly). Instead of selecting from all the vertices, Algorithm 1 can be applied to select feature points from pre-defined anatomical landmarks, whose positions can be measured on the given subject without ambiguity. Figure 10 shows the most informative feature points (with $n_f = 5, 10, 20, 30$ respectively) selected from the 67 well-defined anatomic landmarks by Algorithm 1.

6.1.2 Sparse shape reconstruction

In this section, the selected feature points are used as the markers in sparse shape reconstruction. The positions of the feature points \mathbf{f} on the testing shapes are measured and a new shape $\tilde{\mathbf{S}}_i^{test} = \bar{\mathbf{S}} + \Psi\tilde{\mathbf{w}}(\mathbf{f})$ is constructed by the statistical shape model. The shape parameters $\tilde{\mathbf{w}}$ are estimated by equation (21) by the feature points \mathbf{f} . The surface deviation between the reconstructed shape and the original shape is used to evaluate the quality of

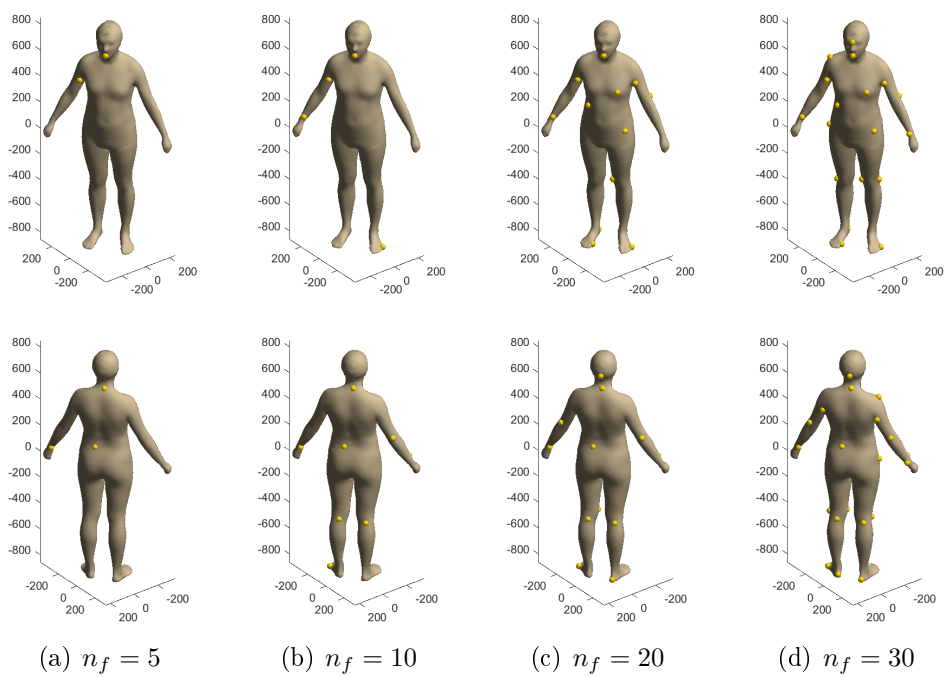


Figure 10: Feature points selected from the anatomic landmarks: (a) 5 feature points; (b) 10 feature points; (c) 15 feature points; (d) 20 feature points. The upper and lower rows show the front and back views. Unit is millimeter.

the reconstruction. The mean surface deviation is calculated as below:

$$d_i = \frac{1}{n_v} \sum_{j=1}^{n_v} \|\mathbf{v}_j^{test_i} - \tilde{\mathbf{v}}_j^{test_i}\|, \quad i = 1, \dots, 216, \quad (36)$$

where $\mathbf{v}_j^{test_i}$ is the position of a vertex on the i th testing shape, $\tilde{\mathbf{v}}_j^{test_i}$ is the position of the vertex on the reconstructed shape.

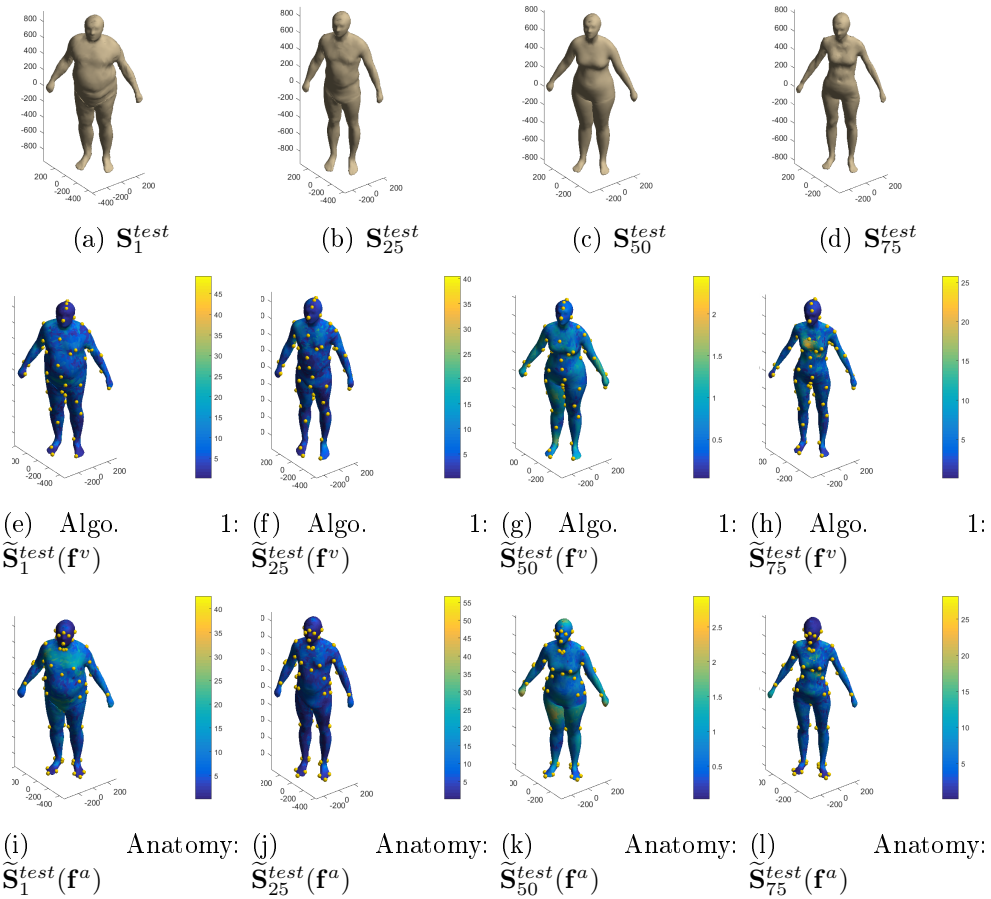


Figure 11: Sparse shape reconstruction by the selected feature points. Top row: the test shapes; middle row: the shapes reconstructed by the 67 feature points \mathbf{f}^v selected by Algorithm 1 from the 6449 vertices; bottom row: the shapes reconstructed by the 67 anatomical landmarks \mathbf{f}^a . The color shows the value of surface deviation. Unit is millimeter.

Figure 11 shows the results of sparse shape reconstruction by the 67 feature points selected from the 6449 vertices (middle row) and by the 67 anatomical landmarks (bottom row). It can be seen that the maximum

surface deviations in the middle row are smaller than that of the bottom row.

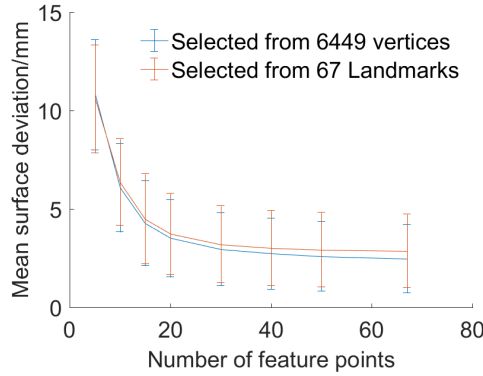


Figure 12: The mean surface deviations of the shape reconstructions with different number of feature points. Red curve: shape reconstructions by the feature points \mathbf{f}^v selected from the 6449 vertices; Blue curve: shape reconstructions by the feature points \mathbf{f}^a selected from the 67 anatomical landmarks. Unit is millimeter.

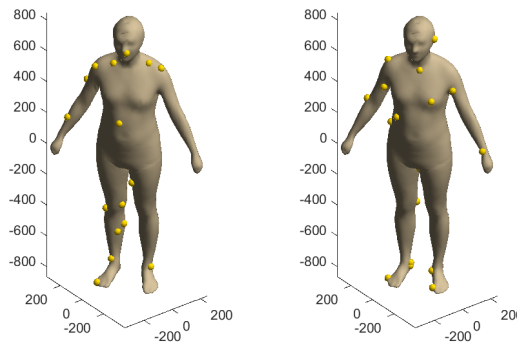
As shown in Figure 12 are the mean surface deviations (36) of the shape reconstructions with different number of feature points. The red color corresponds to the shape reconstructions by the feature points \mathbf{f}^v selected from the 6449 vertices; the blue color corresponds to the shape reconstructions by the feature points \mathbf{f}^a selected from the 67 anatomical landmarks. The red and blue curve in Figure 12 show the average of the mean surface deviations of the reconstructions over the 216 testing shapes: $\bar{d} = \frac{1}{216} \sum_{i=1}^{216} d_i / 216$ with respect to the feature points selected from the 6449 vertices and from the 67 anatomical landmarks. The error bar shows the standard deviation of the mean surface deviation over the 216 testing shapes: $\sqrt{\frac{1}{215} \sum_{i=1}^{216} (d_i - \bar{d})^2}$. It could be seen that as the number of feature points increases, the mean surface deviation decreases. At last, the average of the mean surface deviation is 2.47mm for the red curve and is 2.86mm for the blue curve in Figure 12, which shows the accuracy of the reconstruction.

Table 1 shows the values of the mean surface deviations, where n_f is the number of feature points, $\bar{d}^{(1)}$ is the mean surface deviation of the reconstruction by the feature points selected from all the vertices, $\bar{d}^{(2)}$ is the mean surface deviation of the reconstruction by the feature points selected from the anatomical landmarks.

Table 1: Reconstruction error by different number of feature points: mm

n_f	5	10	15	20	30	40	50	67
$\bar{d}^{(1)}$	10.81	6.08	4.26	3.51	2.95	2.73	2.59	2.47
$\bar{d}^{(2)}$	10.60	6.37	4.50	3.73	3.20	3.02	2.93	2.86

It can be seen that the mean surface deviations in the first row are all smaller than that in the second row except for the case of $n_f = 5$. That's because the feature points of the first row are selected from a much larger pool than that of the second row. This also demonstrates the effectiveness of Algorithm 1, since the selected feature points in the first row are more powerful than the expert defined anatomical landmarks. For the case of $n_f = 5$, the mean surface deviation in the first row is slightly larger (10.81mm vs 10.60mm) than that in the second row, this is because firstly Algorithm 1 is a greedy algorithm and is sensitive to initialization, and secondly, the 67 anatomical landmarks are also meaningful and informative points that well represent the human body shape and are obtained by experts in anthropometry. When selecting just a few feature points (e.g. $n_f = 5$), the 67 anatomical landmarks may be good candidates to select from.



(a) Randomly generated from the 6449 vertices
 (b) Randomly generated from the anatomical landmarks

Figure 13: The 20 feature points randomly generated from (a) the 6449 vertices, (b) the 67 anatomical landmarks. Unit is millimeter.

To further validate the capability of the feature points selected from the 6449 vertices and from the 67 anatomical landmarks, their performances in sparse shape reconstruction are compared with 100 sets of points randomly generated from the 6449 vertices and from the 67 anatomical landmarks

respectively. Figure 13 shows two examples of randomly generated feature points.

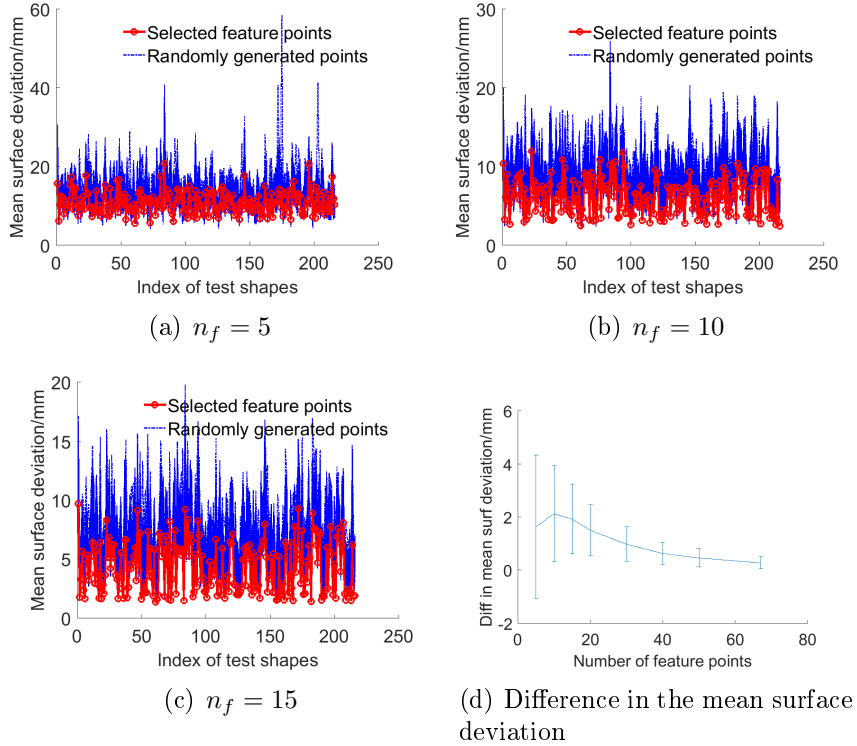


Figure 14: Mean surface deviations of the reconstructions of the 216 testing shapes by the selected feature points (Algorithm 1) and by the 100 sets of randomly generated feature points: (a) 5 feature points; (b) 10 feature points; (c) 15 feature points; (d) difference in the mean surface deviations (the reference is Algorithm 1). Both of the points are selected from the 6449 vertices.

Figure 14 shows the mean surface deviations of the human shape reconstructions obtained by the selected feature points (Algorithm 1) and by the 100 sets of randomly generated feature points. Both of the feature points are selected from the 6449 vertices. It can be seen that the errors of the human shape reconstructions obtained by the selected feature points (Algorithm 1) are smaller than that by the randomly generated feature points. The error curves (red) of the feature points selected by Algorithm 1 stay at the bottom of all the errors curves in Figure 14(a), 14(b) and 14(c). Figure 14(d) shows the differences in the mean surface deviations of the human shape reconstructions obtained by the selected feature points (Algorithm 1) and by the randomly generated points. The curve shows the average difference over the 216 testing shapes and over the 100 set of randomly generated

points: $\frac{1}{100} \sum_j^{\frac{1}{216}} \sum_{i=1}^{216} (d_i^{random_j} - d_i)$, the error bar shows the standard deviation of $d_i^{random_j} - d_i$, where d_i is the mean surface deviation of the i th testing shape reconstructed based on the feature points selected by Algorithm 1 and $d_i^{random_j}$ is the mean surface deviation of the i th testing shape reconstructed based on the j th set of randomly generated feature points. It can be seen that the shape reconstructions obtained by the feature points selected by Algorithm 1 are more precise than that by the randomly generated feature points. However, as the number of feature points increases, the difference becomes smaller. That is due to the compactness of the statistical shape model (the first 39 eigen-modes captures more than 99% of the total shape variance), so we don't need too many feature points to capture the major shape variance in the population. Some of the feature points will become redundant as the number of feature points increases.

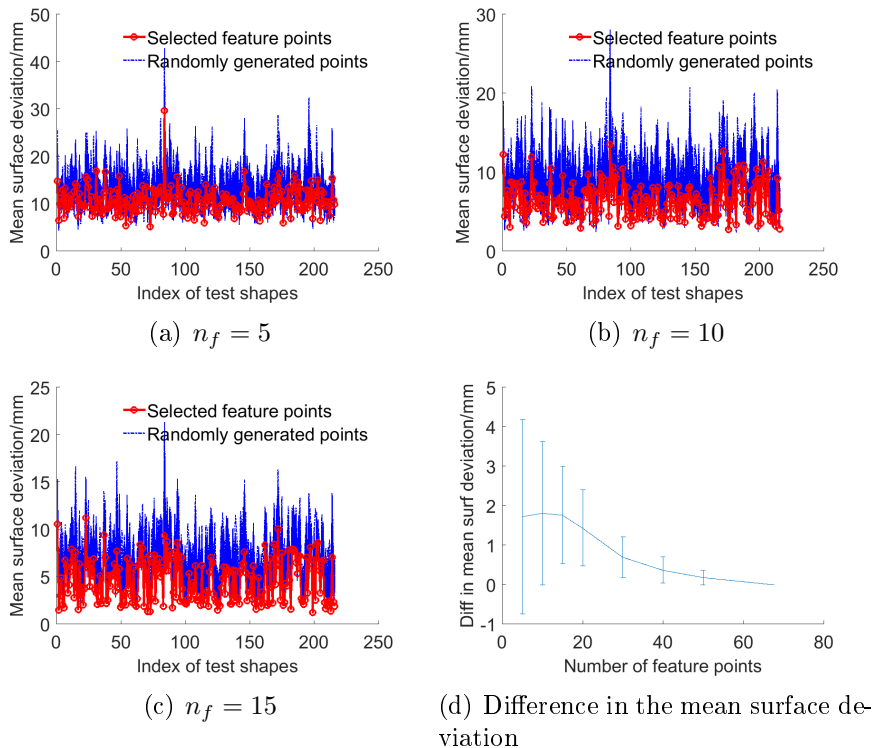


Figure 15: Mean surface deviations of the reconstructions of the 216 testing shapes by the selected feature points (Algorithm 1) and by the 100 sets of randomly generated points: (a) 5 feature points; (b) 10 feature points; (c) 15 feature points; (d) difference in the mean surface deviations (the reference is Algorithm 1). Both of the points are selected from the anatomical landmarks.

Figure 15 shows the mean surface deviations of the human shape reconstructions obtained by the selected feature points (Algorithm 1) and by the 100 sets of randomly generated feature points. Both of the feature points are selected from the 67 anatomical landmarks. It can be seen that the errors of the human shape reconstructions obtained by the selected feature points (Algorithm 1) are smaller than that by the randomly generated feature points. The error curves (red) of the feature points selected by Algorithm 1 stay at the bottom of all the errors curves in Figure 15(a), 15(b) and 15(c). Figure 15(d) shows the differences in the mean surface deviations of the human shape reconstructions obtained by the selected feature points (Algorithm 1) and by the randomly generated points. The curve shows the average difference over the 216 testing shapes and over the 100 sets of randomly generated points, the error bar shows the standard deviation of the differences. It can be seen that the shape reconstructions obtained by the feature points selected by Algorithm 1 are more precise than that by the randomly generated points.

6.1.3 Dimension construction and selection

The 12 most important feature points (the percentage variance captured = 96.8%) selected from the 67 anatomical landmarks are used for dimension construction. Based on which $C_{12}^2 = 66$ lengths and $3C_{12}^3 = 660$ angles are constructed. Combined with the 25 dimensions from the traditional measurement list:

- Circumferences: ankle circ, chest girth, chest circ under bust, head circ, waist circ, vertical trunk circ, hand circ, neck base circ, hip circ maximum, thigh circ maximum, hip circ maximum height.
- Lengths: stature, foot length, arm length (spine-shoulder), arm length (spine-elbow), arm length (spine-wrist), head length, bizygomatic breadth, head breadth, waist height preferred, shoulder (bideltoid) breadth, crotch height, buttock-knee length, face length, hip breadth.

We have a pool of 751 dimensions: $\mathbb{P} = \{l_1 \dots l_{751}\}$. Figure 16 shows the 25 dimensions from the traditional measurement list.

In this section, the dimensions that are selected by expert and by Algorithm 2 are compared. The 4092 training shapes are used to select meaningful dimensions among the population. The 216 testing shapes are used to test the selected dimensions in shape synthesis (28). The dimensions are firstly selected from just the traditional measurement list, whose results are then compared with the selections from the big pool $\mathbb{P} = \{l_1 \dots l_{751}\}$, which includes the constructed dimensions.

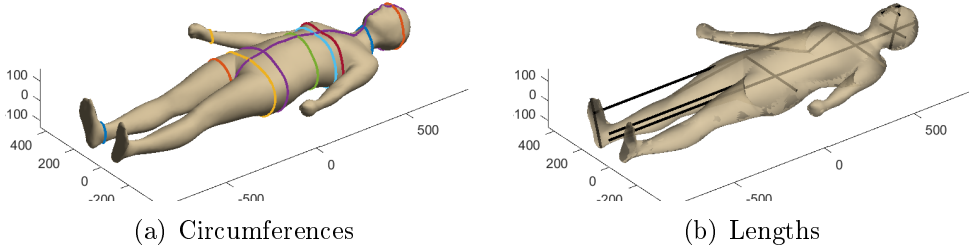


Figure 16: Dimensions from the traditional measurement list: (a) the 11 circumferences; (b) the 14 lengths. Unit is millimeter.

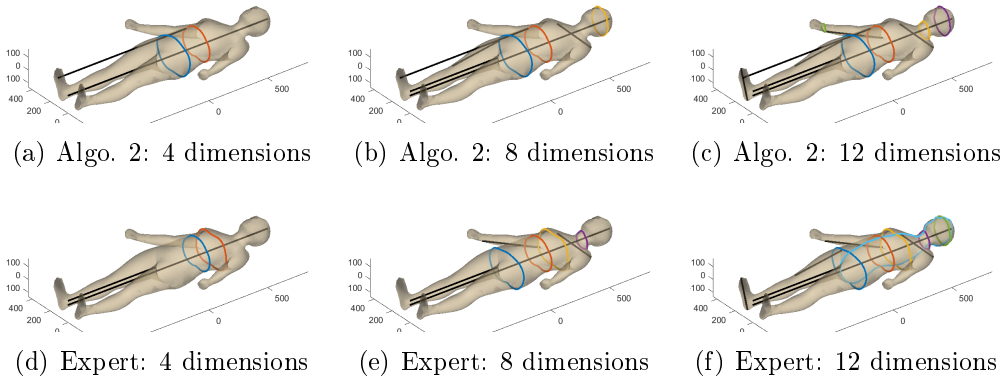


Figure 17: Dimension selection from the traditional measurement list. Unit is millimeter.

Figure 17 shows the results of dimension selection from the traditional measurement list. Two selection approaches are used: dimension selection by Algorithm 2 and dimension selection by expert.

The first column shows the most important 4 dimensions selected by the two approaches. The dimensions selected by Algorithm 2 are: the height of the body, the waist, the circumference of the buttock, and the height of the waist. The dimensions selected by expert are: the height of the body, the waist, the circumference of the chest, and the height of the crotch. The second and third columns show the most important 8 dimensions and 12 dimensions selected by the two approaches.

Figure 18 shows the errors of shape reconstructions of the 216 testing shapes by the dimensions selected from the traditional list. Figure 18(a) shows the errors of shape reconstructions by the dimensions selected by Algorithm 2. Figure 18(b) shows the differences in the shape reconstructions by the expert selected dimensions and by the dimensions selected by Algorithm 2. It could be seen that Algorithm 2 gives slightly smaller mean surface

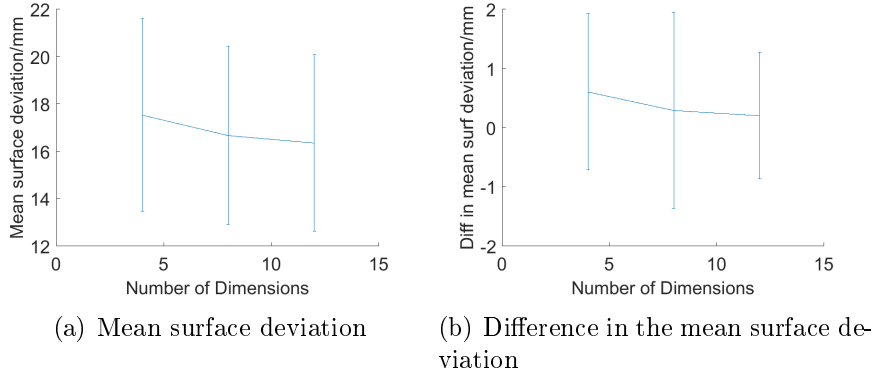


Figure 18: Reconstruction errors with different numbers of dimensions selected from the traditional list: (a) mean surface deviations of the reconstructions by the dimensions selected by Algorithm 2; (b) differences in the mean surface deviations of the reconstructions by the dimensions selected by Algorithm 2 and by expert (the reference is Algorithm 2). The unit is millimeter.

deviations, in a difference of about 0.5mm. Though such a difference is not significant, it shows that at least the proposed algorithm can find as good dimensions as found by the expert, especially considered that the dimension pool only has 25 dimensions. One thing observed is that the reconstruction error doesn't decrease much as we increase the number of dimensions in Figure 18(a). This means that some of shape variations in the population are not captured by the list of traditional measurements and new dimensions need to be constructed, which is better illustrated by Figure 19.

Figure 19 shows the confidence region of the conditional distributions of the shape parameters in the training set, which is obtained from equation (27). The red point shows the true shape parameter of the testing shape being investigated. It can be seen that as the number of dimensions increases, the area of the confidence region of $p(w_1, w_2 | \mathbf{L})$ decrease obviously, which means that the information provided by the additional dimensions can effectively localize the first two shape parameters of the unknown testing shape. However, the area of the confidence region of $p(w_3, w_4 | \mathbf{L})$ barely decreases, which means that the information provided by the additional dimensions are not relevant.

Figure 20 shows the results of dimension selection from the combined pool \mathbb{P} , which contains 751 dimensions (25 from the traditional measurement list and 726 constructed from the selected feature points). The first column shows the most important 4 dimensions. It can be seen that the lengths from the nose to both hands are selected from the list of constructed dimensions.

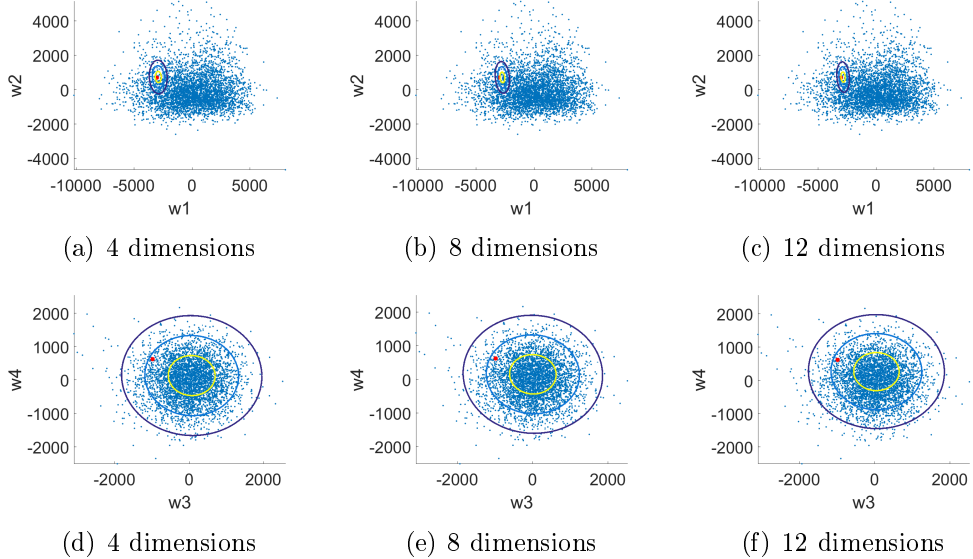


Figure 19: Confidence regions (66%, 90%, 99%) of the conditional distributions $p(w_1, w_2 | \mathbf{L})$ (upper row) and $p(w_3, w_4 | \mathbf{L})$ (bottom row). The red point shows the true shape parameter of the testing shape being investigated. Unit is millimeter.

The second and third columns show the most important 8 dimensions and 12 dimensions selected from the combined pool \mathbb{P} . It can be seen that some angles are selected, which are constructed by the line segments connecting the feature points. The angles can be computed by the edge lengths of the corresponding triangles. The edge lengths can be precisely measured by vernier caliper, since the feature points are selected from well-defined anatomical landmarks.

Figure 21 shows the reconstructions by the selected dimensions. The first row shows the shapes reconstructed by the expert selected dimensions, the second row shows the shapes reconstructed by the dimensions selected from the combined pool. It can be seen that the shapes reconstructed by the dimensions selected from the combined pool by Algorithm 2 have smaller surface deviations.

Figure 22 shows the errors of shape reconstructions of the 216 testing shapes by the dimensions selected from the combined pool \mathbb{P} by Algorithm 2. It could be seen that the reconstruction error deceases linearly as the number of dimensions increases, and is much smaller than the errors in Figure 18, where the dimensions are only selected from the traditional list.

Figure 23 shows the confidence region of the conditional distributions of the shape parameters. It can be seen that as the number of dimen-

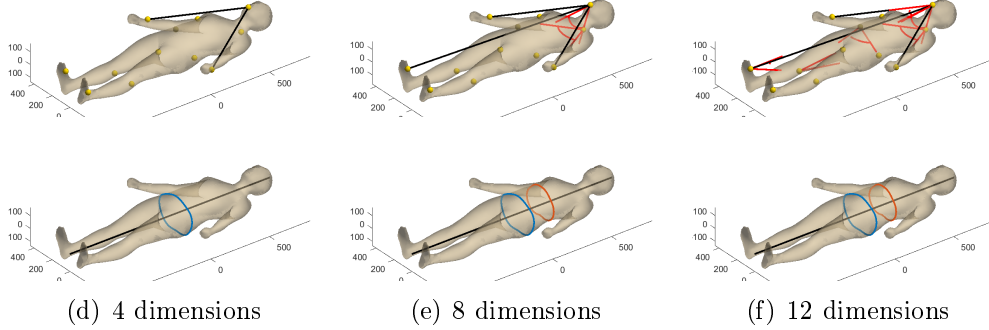


Figure 20: Dimensions selected from the combined pool \mathbb{P} by Algorithm 2: (a) the 4 most important dimensions, (b) the 8 most important dimensions, (c) the 12 most important dimensions. The dimensions in the upper row are the constructed lengths and angles, the dimensions in the lower row are the traditional measurements. Unit is millimeter.

sions increases, the areas of the confidence regions of both $p(w_1, w_2 | \mathbf{L})$ and $p(w_3, w_4 | \mathbf{L})$ decrease obviously, which means that the information provided by the additional dimensions can effectively localize the shape parameters, including the third and fourth shape parameter, of the unknown testing shape. That demonstrates the necessity and effectiveness of the new dimensions constructed by the feature points.

6.2 The rabbit tibia example

The rabbit tibia models are used to demonstrate shape classification by sparse measurements. The database is come from [20]. As show in Figure 24(a) there are 64 rabbit tibias, among which 32 are normal tibias and 32 had surgery on the proximal part. The tibias are scanned 8 weeks after the surgery. It is know from [20] that the surgery do affect the growth of the rabbit tibias. In this study we want to extract the dimensions on the tibia shape that can effectively distinguish the surgical tibias and the normal tibias. The selected dimensions will be used in future studies of surgical effects since it can effectively capture the shape differences caused by the surgery.

6.2.1 Statistical shape modeling

Statistical shape modeling is used to extract the population information of the rabbit tibias. The iterative free form deformation approach [26, 8, 35] is applied in the shape registration of the rabbit tibias. Since the shapes of

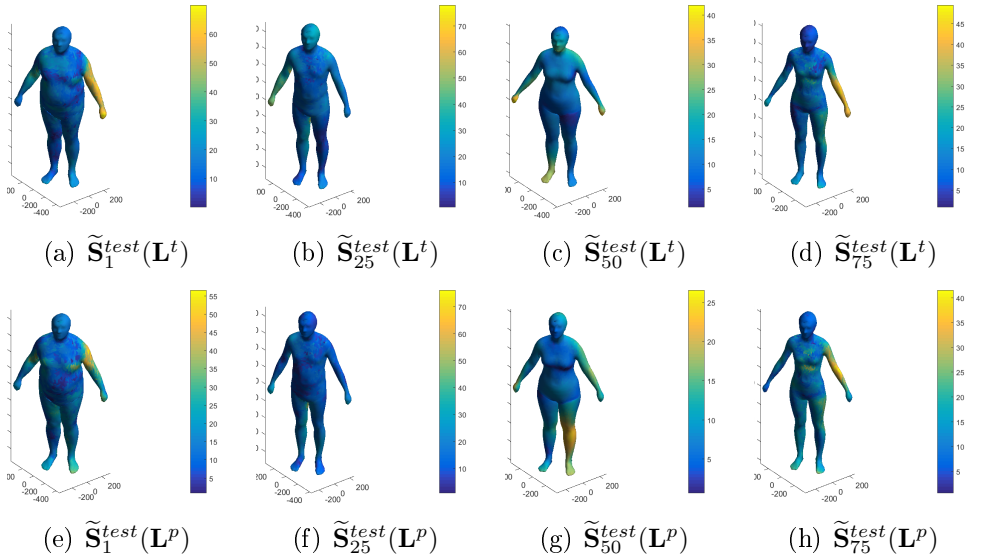


Figure 21: Shape reconstructions by the selected dimensions. The first row shows the shapes reconstructed by the expert selected dimensions \mathbf{L}^t , the second row shows the shapes reconstructed by the dimensions selected from the combined pool \mathbf{L}^p . Unit is millimeter.

the rabbit tibias are all close to each other (as shown in Figure 24(b)), no landmarks are used to guide the registration process.

Figure 24(b) shows the aligned shapes and Figure 24(c) shows the mean shape of the population. Figure 25 shows the results of principal component analysis. It can be seen that the first mode is about the overall size change, the second mode is related to the thickening and elongation of the back of the tibia head, and the third mode is focused on some local shape changes.

The paired student t-test is conducted for each shape parameter between the surgical and the normal tibias. The null hypothesis is that there's no difference between the surgical and normal tibias in terms of the shape parameters. The significance level is chosen at 0.05, and a p-value less than 0.05 means that the probability of the null hypothesis being true is less than 0.05.

By calculating the p-values of the 27 shape parameters we have $p_1 = 0.0045$, $p_2 = 0$, $p_3 \dots p_{27} > 0.05$, which means that the surgical and normal tibias differ along the first and second eigen-modes, which is in accordance with [20].

Figure 26(a) shows the variance of the shape population captured by the increasing number of eigenmodes. Figure 26(b) shows the distribution of the first two shape parameters. It can be seen that the first two shape parameters

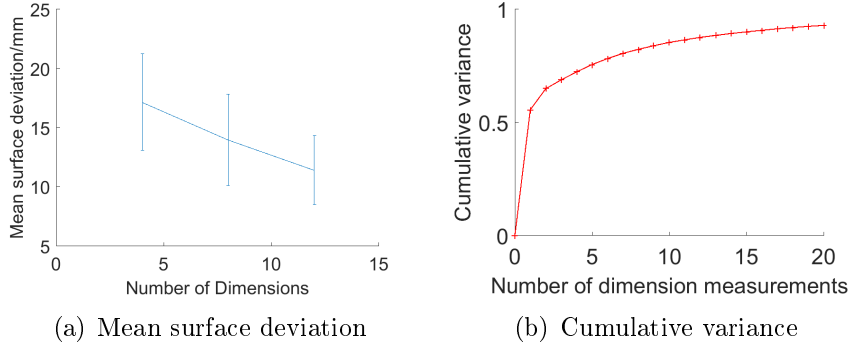


Figure 22: Dimension selection from the combined pool by Algorithm 2: (a) the mean surface deviations of shape reconstructions with different number of dimensions, (b) the percentage variance in the training shapes captured by the increasing number of dimensions.

nicely distinguish the surgical and the normal tibias. However, in real clinical situations, it is very time consuming to obtain the full 3D shapes. Instead, we'd like to extract the dimensions related to the first two eigen-modes that can be measured efficiently in clinical settings.

6.2.2 Feature point identification

Firstly, the feature points that can capture the total variance in the shape population are extracted. Figure 27 shows the results of the feature point selection and the variance of the shape population captured by the increasing number of feature points. In this example, due to the lack of anatomical information, the feature points are selected from all the vertices on the model. This is one limitation of this method since the positions of some of the feature points are hard to precisely measure (e.g. the ones in smooth regions).

6.2.3 Dimension construction and selection

Based on the selected feature points, $C_{15}^2 = 105$ lengths and $3C_{15}^3 = 1365$ angles are constructed. The dimension pool contains 1470 dimensions

$$\mathbb{P} = \{l_1, l_2, \dots, l_{1470}\}.$$

The conditional variance of the distribution $p(w_1, w_2 | \mathbf{L})$ is used to select the dimensions as in equation (33), since we only care about how much variance in w_1, w_2 are captured by the selected dimensions, where w_1, w_2 are the shape parameters that are relevant to the surgical effects.

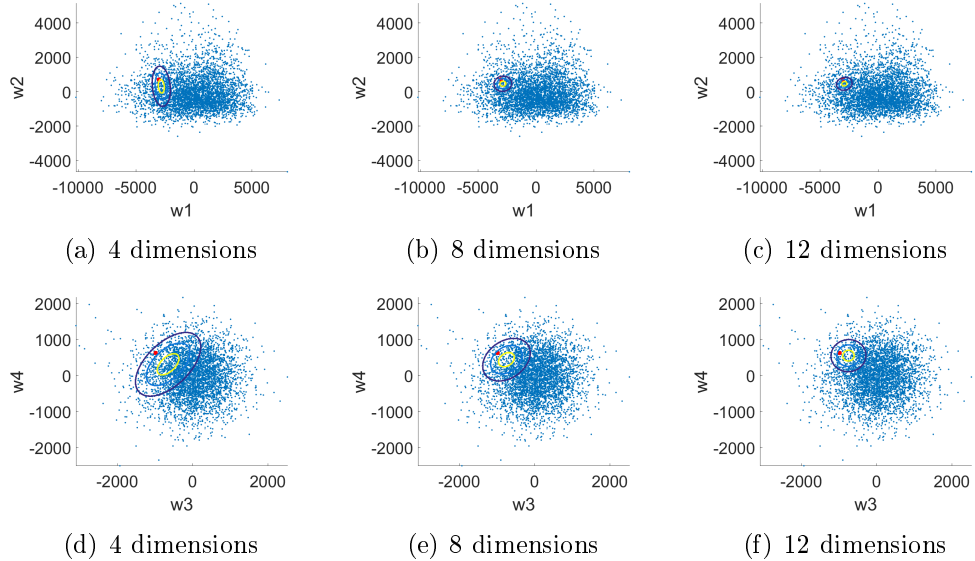


Figure 23: Confidence regions (66%, 90%, 99%) of the conditional distributions $p(w_1, w_2 | \mathbf{L})$ (upper row) and $p(w_3, w_4 | \mathbf{L})$ (bottom row). The red point shows the true shape parameter of the testing shape being investigated. Unit is millimeter.

The selected dimensions are shown in Figure 28. The rank of the selected dimensions is shown by the number in Figure 28(a). The percentage variance of the shape parameters w_1, w_2 captured by the increasing number of dimensions is shown in Figure 28(b). The distribution of the selected dimensions over the groups is shown in Figure 28(c). It can be seen that the selected dimensions are powerful in distinguish the control and surgical tibias compared with merely using the overall length as in [20]. The surgical shapes have smaller head angles (l_2) compared with the control shapes. The selected angle has successfully captured the variation of the second mode, which is very important in distinguishing the two groups of shapes.

Figure 29 shows the dimensions on one control shape and on the corresponding surgical shape. It can be seen that the back of the head of the surgical shape has been thickened and elongated, so the corresponding triangle is also elongated and thus the head angle becomes smaller.

7 Conclusion

This paper proposes a statistical shape model based pipeline to select features points on 3D shapes. Unlike traditional approaches that focus on capturing

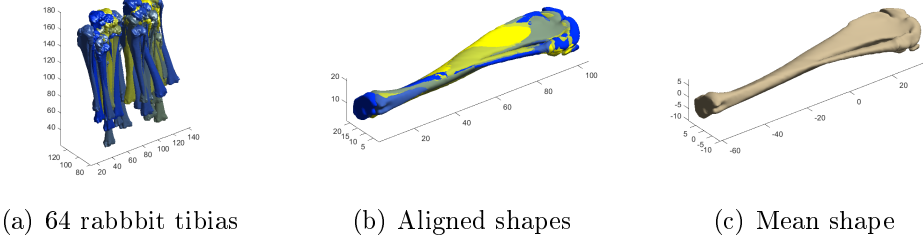


Figure 24: Rabbit tibiae: (a) the 64 training shapes; (b) the aligned shapes; (c) the mean shape. Unit is millimeter.

the geometric information of a single shape, we focus on capturing the population information of a group of shapes. The feature points are selected and ranked by the amount of percentage variance they capture of the shape population.

We then demonstrate the successful incorporation of the proposed feature point identification approach in the applications of sparse shape reconstruction, construction and selection of new dimensions and shape classification by sparse measurements. The numerical results demonstrate the efficiency and effectiveness of the proposed approach.

The contributions of this paper are:

- 1) A metric to quantitatively evaluate the percentage variance of the shape population captured by the feature points.
- 2) Selecting feature points and sizing dimensions by the total variance they capture of the shape population.

The selected feature points and sizing dimensions are capable of capturing the shape variations that are not captured by the anatomical landmarks and traditional list of dimensions. The ability of capturing population information makes the selected feature points and dimensions powerful in sparse shape reconstruction and parametric shape synthesis. For example, with the 67 selected feature points, the mean surface deviation of the reconstructions is 2.47 millimeter, while with the 67 anatomical landmarks, the mean surface deviation is 2.86 millimeter. With the 15 selected feature points, the mean surface deviation of the reconstructions is 4.26 millimeter while the mean surface deviation of the reconstructions by the randomly generated points is 6.1 millimeter.

- 3) A way to automatically construct and select new sizing dimensions.

The new dimensions are automatically composed by the lengths and angles constructed from the selected feature points. It has been shown that the new dimensions are able to capture shape variations in the population that

7 CONCLUSION

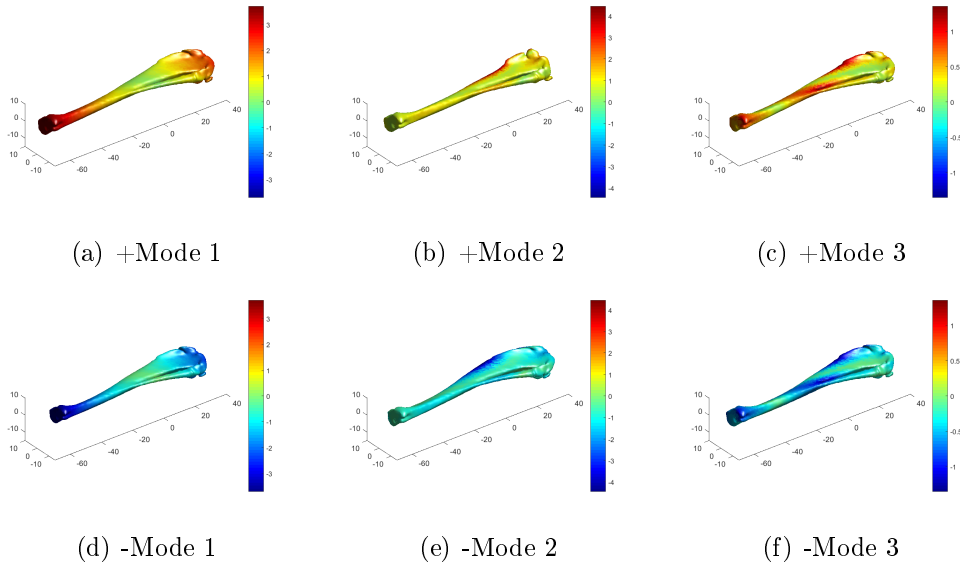


Figure 25: Statistical shape modeling of the rabbit tibias: the first three eigenmodes. Color shows the surface deviation from the mean shape, unit is millimeter.

are not captured by the traditional list of measurements.

4) A way to select dimensions to capture particular shape variations in the population.

In shape classification, shape parameters that are relevant to group differences are identified by paired-t test. The corresponding dimensions are selected to capture the variances in such shape parameters. The numerical results show that the selected dimensions can successfully distinguish the surgical and non-surgical groups.

In the future, we will account for more general shape populations that may not be normally distributed. In this work, the shape parameters are assumed to be normally distributed. For shape populations that are not normally distributed, especially when obvious pose changes are involved [36, 37], alternative techniques for statistical shape learning can be considered such as the support vector machine (SVM), Gaussian process latent variable models (GPLVMs), and neural networks. More general shape registration technique that deals with both shape and pose changes via articulated shape model could also be applied [38].

Our current approach selects feature points (and dimensions) only by considering the amount of shape variations captured by the feature points (and dimensions). However, for many applications, semantic features must present for practical reasons. In the future we will improve the approach

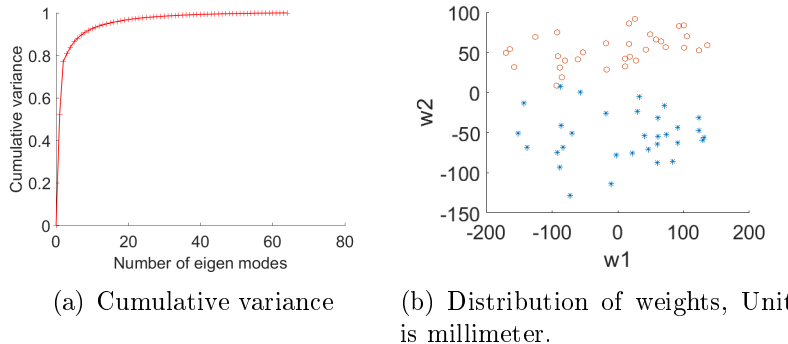


Figure 26: Statistical shape modeling of the rabbit tibias: (a) the cumulative variance captured by the increasing number of eigenmodes; (b) the distribution of the first two shape parameters, $*$: normal, o : surgical.

by considering both the automatically selected feature points and the semantic feature points. The semantic feature points can be selected from the anatomical landmarks and their semantic importance can be determined by comparing with the semantic regions segmented by the approaches in [39, 40].

Accurate shape registration is important to the proposed feature point selection approach. Otherwise unrealistic artifacts would be incorporated in the modes of shape variations and the obtained shape variances would be larger than the actual total variances since the variances of the artifacts are included. In the future, we will evaluate how sensitive this approach is to the quality of shape registration.

References

- [1] Kathleen M Robinette, Sherri Blackwell, Hein Daanen, Mark Boehmer, and Scott Fleming. Civilian american and european surface anthropometry resource (caesar), final report. volume 1. summary. Technical report, DTIC Document, 2002.
- [2] Seung-Yeob Baek and Kunwoo Lee. Statistical foot-shape analysis for mass-customisation of footwear. *International Journal of Computer Aided Engineering and Technology*, 8(1-2):80–98, 2016.
- [3] Xiaobai Chen, Abulhair Saparov, Bill Pang, and Thomas Funkhouser. Schelling points on 3d surface meshes. *ACM Transactions on Graphics (TOG)*, 31(4):29, 2012.

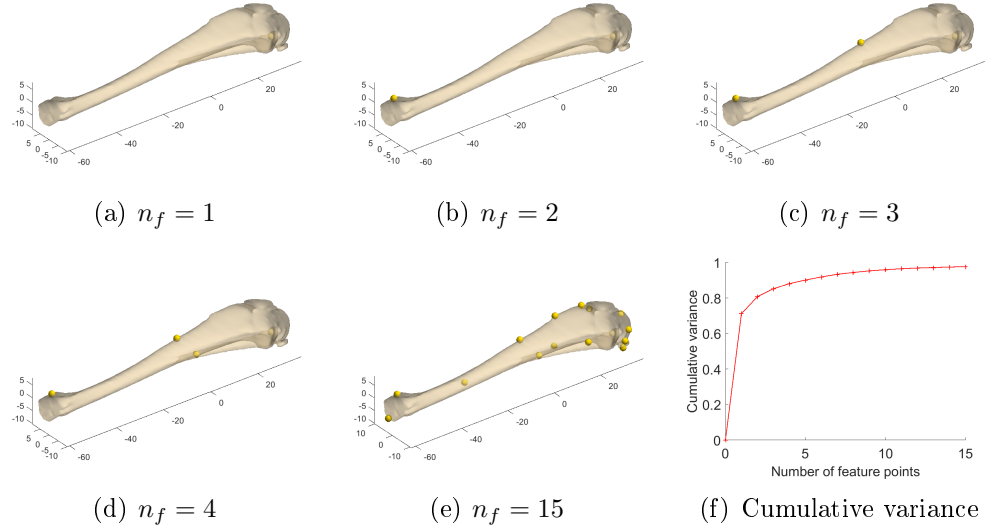


Figure 27: Feature points selection: (a) - (e) the most important 15 feature points selected by Algorithm 1; (f) the cumulative variance captured by the increasing number of feature points. The feature points are selected from the all the vertices on the model. Unit is millimeter.

- [4] Charlie CL Wang. Parameterization and parametric design of mannequins. *Computer-Aided Design*, 37(1):83–98, 2005.
- [5] Chih-Hsing Chu, Ya-Tien Tsai, Charlie CL Wang, and Tsz-Ho Kwok. Exemplar-based statistical model for semantic parametric design of human body. *Computers in Industry*, 61(6):541–549, 2010.
- [6] Weiwei Zhang and Michael Brady. Feature Point Detection for Non-rigid Registration of Digital Breast Tomosynthesis Images. In *Digital Mammography/IWDM*, pages 296–303. Springer, 2010.
- [7] Seung-Yeob Baek and Kunwoo Lee. Parametric human body shape modeling framework for human-centered product design. *Computer-Aided Design*, 44(1):56–67, 2012.
- [8] Xilu Wang and Xiaoping Qian. A statistical atlas based approach to automated subject-specific FE modeling. *Computer-Aided Design*, 70:67–77, 2016.
- [9] Brett Allen, Brian Curless, and Zoran Popović. The space of human body shapes: reconstruction and parameterization from range scans. In *ACM transactions on graphics (TOG)*, volume 22, pages 587–594. ACM, 2003.

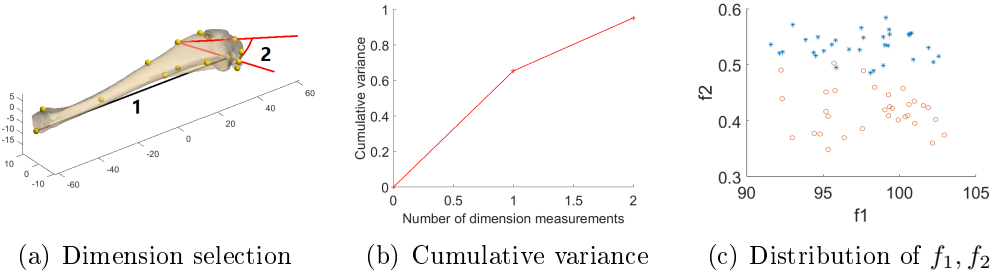


Figure 28: Dimension selection: (a) the 2 dimensions that are most relevant to the surgical effects; (b) the variance in the first shape parameters w_1, w_2 captured by the increasing number of dimensions; (c) the distribution of the selected dimensions over the 64 tibias. *: normal, o: surgical.

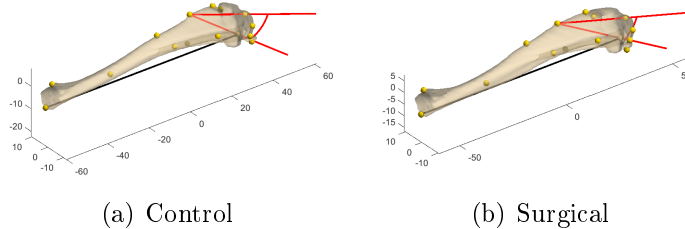


Figure 29: Comparing the sizing dimensions on: (a) the control shape; (b) the surgical shape. Unit is millimeter.

- [10] Volker Blanz, Albert Mehl, Thomas Vetter, and H-P Seidel. A statistical method for robust 3D surface reconstruction from sparse data. In *3D Data Processing, Visualization and Transmission, 2004. 3DPVT 2004. Proceedings. 2nd International Symposium on*, pages 293–300. IEEE, 2004.
- [11] Chun-Yang Tseng, I-Jan Wang, and Chih-Hsing Chu. Product personalization using 3d parametric face models: An example of the eye-glass frame design. In *ASME 2015 International Design Engineering Technical Conferences and Computers and Information in Engineering Conference*, pages V01BT02A018–V01BT02A018. American Society of Mechanical Engineers, 2015.
- [12] David Cohen-Steiner, Pierre Alliez, and Mathieu Desbrun. Variational shape approximation. In *ACM Transactions on Graphics (TOG)*, volume 23, pages 905–914. ACM, 2004.
- [13] Sagi Katz, George Leifman, and Ayellet Tal. Mesh segmentation using

- feature point and core extraction. *The Visual Computer*, 21(8-10):649–658, 2005.
- [14] Vladislav Kraevoy and Alla Sheffer. Cross-parameterization and compatible remeshing of 3d models. In *ACM Transactions on Graphics (TOG)*, volume 23, pages 861–869. ACM, 2004.
 - [15] Tsz-Ho KwoK, Yunbo Zhang, and Charlie CL Wang. Efficient optimization of common base domains for cross parameterization. *IEEE Transactions on Visualization and Computer Graphics*, 18(10):1678–1692, 2012.
 - [16] Timor Kadir and Michael Brady. Saliency, scale and image description. *International Journal of Computer Vision*, 45(2):83–105, 2001.
 - [17] Chang Ha Lee, Amitabh Varshney, and David W Jacobs. Mesh saliency. In *ACM transactions on graphics (TOG)*, volume 24, pages 659–666. ACM, 2005.
 - [18] Dragomir Anguelov, Praveen Srinivasan, Daphne Koller, Sebastian Thrun, Jim Rodgers, and James Davis. Scape: shape completion and animation of people. In *ACM Transactions on Graphics (TOG)*, volume 24, pages 408–416. ACM, 2005.
 - [19] Kang Li, Xiaoping Qian, Caitlin Martin, and Wei Sun. Toward patient-specific computational study of aortic diseases: a population based shape modeling approach. In *ASME 2014 International Design Engineering Technical Conferences and Computers and Information in Engineering Conference*, pages V01AT02A080–V01AT02A080. American Society of Mechanical Engineers, 2014.
 - [20] Matthew A Halanski, Tugrul Yildirim, Rajeev Chaudhary, Matthew S Chin, and Ellen Leiferman. Periosteal fiber transection during periosteal procedures is crucial to accelerate growth in the rabbit model. *Clinical Orthopaedics and Related Research®*, 474(4):1028–1037, 2016.
 - [21] Ian L Dryden and Kanti V Mardia. *Statistical Shape Analysis*, volume 4. J. Wiley Chichester, 1998.
 - [22] Mikkel B Stegmann and David Delgado Gomez. A brief introduction to statistical shape analysis. *Informatics and Mathematical Modelling, Technical University of Denmark, DTU*, 15:11, 2002.
 - [23] Paul J Besl and Neil D McKay. Method for registration of 3D shapes. In *Robotics-DL tentative*, pages 586–606. International Society for Optics and Photonics, 1992.

-
- [24] Brian Amberg, Sami Romdhani, and Thomas Vetter. Optimal step Non-rigid ICP algorithms for surface registration. In *Computer Vision and Pattern Recognition, 2007. CVPR'07. IEEE Conference on*, pages 1–8. IEEE, 2007.
 - [25] Haili Chui and Anand Rangarajan. A new point matching algorithm for non-rigid registration. *Computer Vision and Image Understanding*, 89(2):114–141, 2003.
 - [26] Hesheng Wang and Baowei Fei. Non-rigid point registration for 2D curves and 3D surfaces and its various applications. *Physics in medicine and biology*, 58(12):4315, 2013.
 - [27] Rhodri H Davies, Carole J Twining, Tim F Cootes, John C Waterton, and Camillo J Taylor. A minimum description length approach to statistical shape modeling. *Medical Imaging, IEEE Transactions on*, 21(5):525–537, 2002.
 - [28] Kang Li and Xiaoping Qian. Direct diffeomorphic reparameterization for correspondence optimization in statistical shape modeling. *Computer-Aided Design*, 64:33–54, 2015.
 - [29] Emanuele Rodolà, Luca Cosmo, Michael M Bronstein, Andrea Torsello, and Daniel Cremers. Partial functional correspondence. In *Computer Graphics Forum*, volume 36, pages 222–236. Wiley Online Library, 2017.
 - [30] John C Gower. Generalized procrustes analysis. *Psychometrika*, 40(1):33–51, 1975.
 - [31] Isabelle Guyon and André Elisseeff. An introduction to variable and feature selection. *Journal of machine learning research*, 3(Mar):1157–1182, 2003.
 - [32] Natasha Gelfand, Leslie Ikemoto, Szymon Rusinkiewicz, and Marc Levoy. Geometrically stable sampling for the icp algorithm. In *3-D Digital Imaging and Modeling, 2003. 3DIM 2003. Proceedings. Fourth International Conference on*, pages 260–267. IEEE, 2003.
 - [33] Tang K Kwok T. Improvements to the iterative closest point algorithm for shape registration in manufacturing. *Journal of Manufacturing Science and Engineering*, 138(1):011014, 2015.
 - [34] Leonid Pishchulin, Stefanie Wuhrer, Thomas Helten, Christian Theobalt, and Bernt Schiele. Building statistical shape spaces for 3D human modeling. *Pattern Recognition*, 67:276–286, 2017.

- [35] Xilu Wang. *Statistical Shape Modeling for Custom Design and Analysis*. The University of Wisconsin-Madison, 2017.
- [36] Nils Hasler, Carsten Stoll, Martin Sunkel, Bodo Rosenhahn, and H-P Seidel. A statistical model of human pose and body shape. In *Computer Graphics Forum*, volume 28, pages 337–346. Wiley Online Library, 2009.
- [37] Keith Gochow, Steven L Martin, Aaron Hertzmann, and Zoran Popović. Style-based inverse kinematics. In *ACM transactions on graphics (TOG)*, volume 23, pages 522–531. ACM, 2004.
- [38] David A Hirshberg, Matthew Loper, Eric Rachlin, and Michael J Black. Coregistration: Simultaneous alignment and modeling of articulated 3D shape. In *European Conference on Computer Vision*, pages 242–255. Springer, 2012.
- [39] Ruizhen Hu, Lubin Fan, and Ligang Liu. Co-Segmentation of 3D Shapes via Subspace Clustering. In *Computer Graphics Forum*, volume 31, pages 1703–1713. Wiley Online Library, 2012.
- [40] Oana Sidi, Oliver van Kaick, Yanir Kleiman, Hao Zhang, and Daniel Cohen-Or. *Unsupervised co-segmentation of a set of shapes via descriptor-space spectral clustering*, volume 30. ACM, 2011.